**Diogo Filipe Monrroy Vilan e Melo**

Licenciado em Bioquímica

# Structure based reaction mechanism studies on periplasmic nitrate reductase

Dissertação para obtenção do Grau de Mestre em Bioquímica

Orientador: Dra. Catarina Coelho, UCIBIO, FCT/UNL
Co-orientador: Prof. Maria João Romão, UCIBIO, FCT/UNL

Júri:

Presidente: Prof. Dr. Ricardo Franco, FCT/UNL
Arguente(s): Dr. José Artur Brito, ITQB/UNL
Vogal(ais): Dra. Catarina Coelho, UCIBIO, FCT/UNL

FACULDADE DE
CIÊNCIAS E TECNOLOGIA
UNIVERSIDADE NOVA DE LISBOA

**Sep. 2017**

**Diogo Filipe Monrroy Vilan e Melo**

Licenciado em Bioquímica

# Structure based reaction mechanism studies on periplasmic nitrate reductase

Dissertação para obtenção do Grau de Mestre em Bioquímica

Orientador: Dra. Catarina Coelho, UCIBIO, FCT/UNL

Co-orientador: Prof. Maria João Romão, UCIBIO, FCT/UNL

Júri:

Presidente: Prof. Dr. Ricardo Franco, FCT/UNL
Arguente(s): Dr. José Artur Brito, ITQB/UNL
Vogal(ais): Dra. Catarina Coelho, UCIBIO, FCT/UNL

FACULDADE DE CIÊNCIAS E TECNOLOGIA
UNIVERSIDADE NOVA DE LISBOA

**Set. 2017**

“Structure based reaction mechanism studies on periplasmic nitrate reductase”

—Copyright‖ em nome de Diogo Filipe Monrroy Vilan e Melo, da FCT/UNL e da UNL

A Faculdade de Ciências e Tecnologia e a Universidade Nova de Lisboa têm o direito, perpétuo e sem limites geográficos, de arquivar e publicar esta dissertação através de exemplares impressos reproduzidos em papel ou de forma digital, ou por qualquer outro meio conhecido ou que venha a ser inventado, e de a divulgar através de repositórios científicos e de admitir a sua cópia e distribuição com objectivos educacionais ou de investigação, não comerciais, desde que seja dado crédito ao autor e editor.

# AGRADECIMENTOS

Agradeço em primeiro lugar à minha orientadora, Catarina Coelho. Foi ela quem teve mais influência em mim e na minha aprendizagem durante este ano que foi sem dúvida, o período de tempo em que mais aprendi até à data (e agradeço a paciência que teve em alguns dos momentos). Foi também o ano em que eu percebi e decidi, querer ser um cristalógrafo!

Agradeço também à minha co-supervisora, Maria João Romão. Sempre que esteve presente colocou-me questões bastante pertinentes que me ajudaram ao longo do percurso, e teve sempre uma atitude extremamente positiva e motivadora.

Agradeço a todas as pessoas do grupo Xtal, ajudaram-me sempre que eu precisei. Agradeço em especial àqueles que contribuíram diretamente para o meu trabalho: Filipe Freire, Cecília Bonifácio, Márcia Correia e Francisco Leisico.

Agradeço à Rita Fernandes e ao meu irmão Ricardo Melo, foram sem dúvida o maior apoio que eu tive durante este ano, em alguns momentos muito difícil. Agradeço muito à minha família, nomeadamente aos meus pais Raul Melo e Paula Vilan, ao José Boieiro, aos meus avós Helena Vilan, Carlos Vilan, Júlia Melo e Francisco Melo. Contribuíram com apoio emocional incondicional, conselhos sábios e apoio financeiro; sem os quais não me teria sido possível seguir este caminho, e poder viver a aventura que me espera para os próximos anos.

Obrigado a todos!

“One should bear in mind that a macromolecular refinement against a high resolution data is never finished, only abandoned.”

- George Sheldrick 2008

# ABSTRACT

The Periplasmic Nitrate Reductase (Nap) from *Cupriavidus necator* (*Cn*) belongs to the Dimethyl Sulfoxide (DMSO) Reductase family of mononuclear Mo-containing enzymes and catalyzes the reduction of nitrate to nitrite. The protein comprises a large catalytic subunit containing the Mo active site and one [4Fe-4S] cluster (NapA, 91kDa), and a small diheme *c-type* cytochrome subunit (NapB, 17kDa). In the present dissertation, the reaction mechanism of the Periplasmic Nitrate Reductase from *Cupriavidus necator* is studied by X-Ray Crystallography and complementary techniques like Thermal Shift Assays (TSA), Isothermal Titration Calorimetry (ITC) and Microscale Thermophoresis (MST).

In the first crystallographic studies of Nap from *Desulfovibrio desulfuricans (Dd)*, it was established that in the active site, the Mo atom was coordinated by two cis-dithioline groups, a sulfur from a cysteine side chain and a water/hydroxo ligand. Recently published crystal structures of Nap, particularly the structure of the heterodimeric *Cn* NapAB solved at high resolution (1.5 Å) and *Dd* NapA with bound ligands demonstrated that the sixth ligand is in fact a sulfur atom, contrary to the previous believed water/hydroxo ligand. Also, a partially reduced NapAB *Cn* crystal structure was obtained, where the coordinating Mo Cys thiolate is partially occupying a new conformation. The sixth sulfur ligand seems to have a partial disulfide bond with the Cys thiolate group, blocking nitrate from interacting directly with the Mo atom unless some rearrangement occurs during catalysis.

Various crystal structures of NapAB from *Cn* co-crystallized with ligands are presented in this dissertation complemented by TSA, ITC and MST results. The results corroborate the existence of an alternate conformation of the coordinating Mo Cys thiolate and pave the way for more studies about the reaction mechanism of nitrate reductases.

# RESUMO

A nitrato reductase periplasmática (Nap) de *Cupriavidus necator (Cn)* pertence à família da Dimetil Sulfóxido (DMSO) Redutase de enzimas mononucleares de Mo e catalisa a redução de nitrato a nitrito. A proteína contém uma grande subunidade catalítica que contém o centro ativo de Mo e um centro [4Fe-4S] (NapA, 91kDa) e uma pequena subunidade de citocromo dihémica tipo c (NapB, 17kDa). Na presente dissertação, o mecanismo de reacção da nitrato redutase periplasmática de *Cupriavidus necator* é estudada por Cristalografia de Raios-X e técnicas complementares como “Thermal Shift Assays” (TSA), “Isothermal Titration Calorimetry” (ITC) and “Microscale Thermophoresis” (MST).

Nos primeiros estudos cristalográficos da Nap de *Desulfovibrio desulfuricans (Dd)*, estabeleceu-se que no centro ativo o átomo de Mo seria coordenado por dois grupos cis-ditiol, um enxofre de uma cadeia lateral de cisteína e um ligando água/hidroxilo. As estruturas cristalinas recentemente publicadas de Nap, particularmente a estrutura do heterodímero NapAB de *Cn* a alta resolução (1.5 Å) e *Dd* NapA com ligandos, demonstraram que o sexto ligando de Mo é de fato um átomo de enxofre, ao contrário do ligando de hidroxilo / água anteriormente estabelecido. Além disso, obteve-se uma estrutura da NapAB de *Cn* parcialmente reduzida, onde o grupo tiolato da cisteína que coordena  o Mo Cys está a ocupar parcialmente uma nova posição. O sexto ligando de enxofre parece ter uma ligação parcial de dissulfureto com o grupo tiolato da cisteína, bloqueando o nitrato de interagir diretamente com o átomo de Mo, a menos que ocorra algum rearranjo durante a catálise.

Várias estruturas cristalinas da NapAB de *Cn* co-cristalizadas com ligandos são apresentadas nesta dissertação complementadas pelos resultados de TSA, ITC e MST. Os resultados comprovam a existência de uma conformação alternativa da cisteína que coordena o Mo e abre caminho para mais estudos sobre o mecanismo de reação das nitrato redutases.

# TABLE OF CONTENTS

Abstract.......I
Resumo.......III
Table of Contents.......V
Table of Figures.......VII
List of Tables.......IX
Table of Abbreviations.......XI
1 Introduction.......1
  1.1 Molybdenum Enzymes and the Pyranopterin Cofactor.......3
  1.2 Nitrate Reductases.......5
    1.2.1 Biologic and Ecologic Context.......5
    1.2.2 Structure of Periplasmic Nitrate Reductases: State of the Art.......6
    1.2.3 Proposed reaction mechanism and its considerations.......8
  1.3 X-Ray Crystallography.......10
    1.3.1 Protein crystallization.......11
      1.3.1.1 Phase Diagrams and the Crystallization Process.......11
      1.3.1.2 Crystallization Methods.......12
      1.3.1.3 Co-crystallization, Soakings and Cryoprotectant Solutions.......13
    1.3.2 X-Ray Sources.......14
    1.3.3 Protein crystal diffraction.......15
    1.3.4 The Phase problem.......16
    1.3.5 Model Improvement.......17
    1.3.6 Model analysis and validation.......18
  1.4 Isothermal Titration Calorimetry (ITC).......19
  1.5 Thermal Shift Assay (TSA).......20
  1.6 Microscale Thermophoresis (MST).......20
  1.7 Objectives.......21
2 Materials and Methods.......23
  2.1 Protein Purification.......25
  2.2 Protein crystallization.......26
    2.2.1 Screening and optimization.......26
    2.2.2 Co-crystallizations and soakings.......27
  2.3 Data collection, processing and structure determination.......29
    2.3.1 Model Building and Refinement.......30
  2.4 Thermal Shift Assays (TSA).......30
  2.5 Isothermal Titration Calorimetry (ITC).......31

- 2.6 Microscale Thermophoresis (MST) ... 31

3 Results and Discussion ... 33

- 3.1 Protein Purification and activity assays ... 35
- 3.2 Protein Crystallization ... 36
  - 3.2.1 Screening and Optimization ... 36
    - 3.2.1.1 Bis-Tris and Succinic Acid ... 36
    - 3.2.1.2 The JCSG$^+$ screen ... 37
  - 3.2.2 Co-crystallization with reducing agents ... 38
  - 3.2.3 Other co-crystallization and soakings ... 41
- 3.3 Data Diffraction and Model Interpretation ... 42
  - 3.3.1 Oxidized cysteines ... 47
- 3.4 Thermal Shift Assays ... 51
- 3.5 Isothermal Titration Calorimetry ... 53
- 3.6 Microscale Thermophoresis ... 54

4 Conclusions and future perspectives ... 57

5 Bibliography ... 63

# TABLE OF FIGURES

**Figure 1.1:** Pyranopterin Dependent Enzyme Families and the Moco Biosynthesis. ....... 4

**Figure 1.2:** Structure of NapAB from *Cupriavidus necator*. ........................................... 7

**Figure 1.3:** NapAB proposed reaction mechanism........................................................ 9

**Figure 1.4:** A protein crystallization phase diagram. .................................................. 12

**Figure 1.5:** Representations of the principle vapor diffusion method techniques: hanging drop, sitting drop and microbatch. .................................................................... 13

**Figure 1.6:** Schematic representation of the diffraction experiment and constructive interference. ........................................................................................................ 16

**Figure 1.7:** Typical MST experimental results. ........................................................... 21

**Figure 3.1:** Characterization of the NapAB purification. .............................................. 34

**Figure 3.2:** Results from the crystallization screens. .................................................. 36

**Figure 3.3:** Results from crystallization optimization and co-crystallization with DTT, TCEP and potassium nitrate.......................................................................... 38

**Figure 3.4:** Comparison of the different unit cells obtained. ........................................ 42

**Figure 3.5:** Crystal structure of partially reduced Nap and nitrite in nitrate co-crystallized Nap. ............................................................................................................... 45

**Figure 3.6:** Crystal structure of nitrite in nitrate co-crystallized Nap. ............................ 46

**Figure 3.7:** Spectrum of NapAB with sodium dithionite. ............................................... 47

**Figure 3.8:** Crystal structure of Nap zooming the oxidized cysteines 388 and 784 in the subunit NapA........................................................................................................ 48

**Figure 3.9:** Comparison of various TSA results. ......................................................... 51

**Figure 3.10:** Comparison of an ITC assay to the control. ............................................. 52

**Figure 3.11:** Summary of the microscale thermophoresis assays. ................................ 55

# LIST OF TABLES

**Table 2-1 –** Summary of ligands used in the co-crystallization assays: reducing agents, substrates, substrate- analogues and inhibitors. 28
**Table 2-2 –** Summary of different conditions tested for NapAB Cn in TSA. 31
**Table 2-3 -** MST Binding Affinity Assays 32
**Table 3-1 –** Summary of the various NapAB ligands and effects in the co-crystallization experiments. 41
**Table 3-2 –** Summary of the results from the Nap crystals obtained in aerobic conditions and tested in the various synchrotron beamlines. 44
**Table 3-3 –** Summary of the results from the NapAB crystals obtained in anaerobic conditions and tested in the various synchrotron beamlines 45
**Table 3-4 –** Statistics on data collection and structure refinement. 50

# TABLE OF ABBREVIATIONS

---

*Cn – Cupriavidus necator*

CODH – Carbon monoxide Dehydrogenase

Dd – *Desulfovibrio desulfuricans*

DTT – Dithiothreitol

EBDH – Ethylbenzene Dehydrogenase

ESRF – *European Synchrotron Radiation Facility*

Fdh – Formate dehydrogenase

FT – Fourier Transform

GTP – Guanosine-5'-triphosphate

HPLC – High Performance Liquid Chromatography

ITC – Isothermal Titration Calorimetry

MGD – Molybdopterin guanosine dinucleotide

Moco – Molybdenum Cofactor

MPT – Metal Containing Pterin

MST – Microscale Thermophoresis

NADPH – Nicotinamide adenine dinucleotide phosphate

Nap – Periplasmic Nitrate Reductase

Nar – Respiratory Nitrate Reductase

Nas – Assimilatory Nitrate Reductase

NR – Nitrate reductase

PEG – Polyethylene Glycol

RT-PCR – Real Time Polymerase Chain Reaction

SAXS – Small-angle X-ray scattering

SDH – Sulfite Dehydrogenase

SDS – Sodium dodecyl sulfate

SDS-PAGE – Sodium dodecyl sulfate polyacrylamide gel electrophoresis

SO – Sulfite oxidase

TMAOR – Trimethylamine Oxide

XDH – Xanthine Oxidase/Dehydrogenase

XO – Xanthine oxidase

# 1 INTRODUCTION

## 1.1 MOLYBDENUM ENZYMES AND THE PYRANOPTERIN COFACTOR

Molybdenum (Mo) is a transition metal incorporated in more than 50 known enzymes and is essential to almost all known forms of life. Organisms that do not dependent on this element use tungsten (W) instead, which has similar chemical characteristics. [1], [2].

Molybdenum is a versatile element that is able to coordinate from 4 up to 8 ligands, varying in oxidation states from -2 to 6, being oxidation states IV to VI the most stable while bonded to biologic macromolecules. This flexibility in oxidation states allows it to act as transducer between obligatory two-electron and one-electron oxidation-reduction systems [1]. Mo is mainly available in seawater as molybdate ($MoO_4^{2-}$) and is found either in the multinuclear MoFe7 (bacterial nitrogenases) or mononuclear (bond to one or more pterin cofactor) forms [3], [4].

Mononuclear Mo enzymes possess a tricyclic pterin (or pyranopterin) cofactor, originally named Moco (Molybdenum Cofactor) and it was first discovered in xanthine dehydrogenase (XDH) and nitrate reductase (NR) enzymes. Only later it was found that it also binds tungsten. Mo is found coordinating the dithiolene group of either one (xanthine oxidase and sulfite oxidase families – XO and SO respectively) or two (dimethyl sulfoxide reductase family - DMSO) pyranopterins. Besides binding to the pyranopterin, Mo is also found coordinated to terminal oxo/hydroxo groups, sulfide groups and amino acid residues side chains through different combinations. Based on the Mo ligands, spectroscopic and biochemical data, pyranopterin-dependent enzymes have been divided into three families: the xanthine oxidase (XO), the sulfite oxidase (SO) and the DMSO reductase families (**Figure 1.1.a**). In the XO and SO families, only one pyranopterin coordinates the Mo atom. Additionally, in the XO family the Mo is found coordinating a hydroxyl group, one oxygen and a sulfur while in the SO family Mo binds to one hydroxyl group, an oxygen and to the side chain of a cysteine. In the DMSO reductase family two pyranopterins coordinate the Mo atom which also coordinates one hydroxyl or thiol groups, oxygen or sulfur atoms and the side chains of: cysteine, selenocysteine, aspartic acid or serine [5]. DMSO is the most diverse family and is further divided into three subfamilies as depicted in **Figure 1.1.a**. [3], [5], [6].

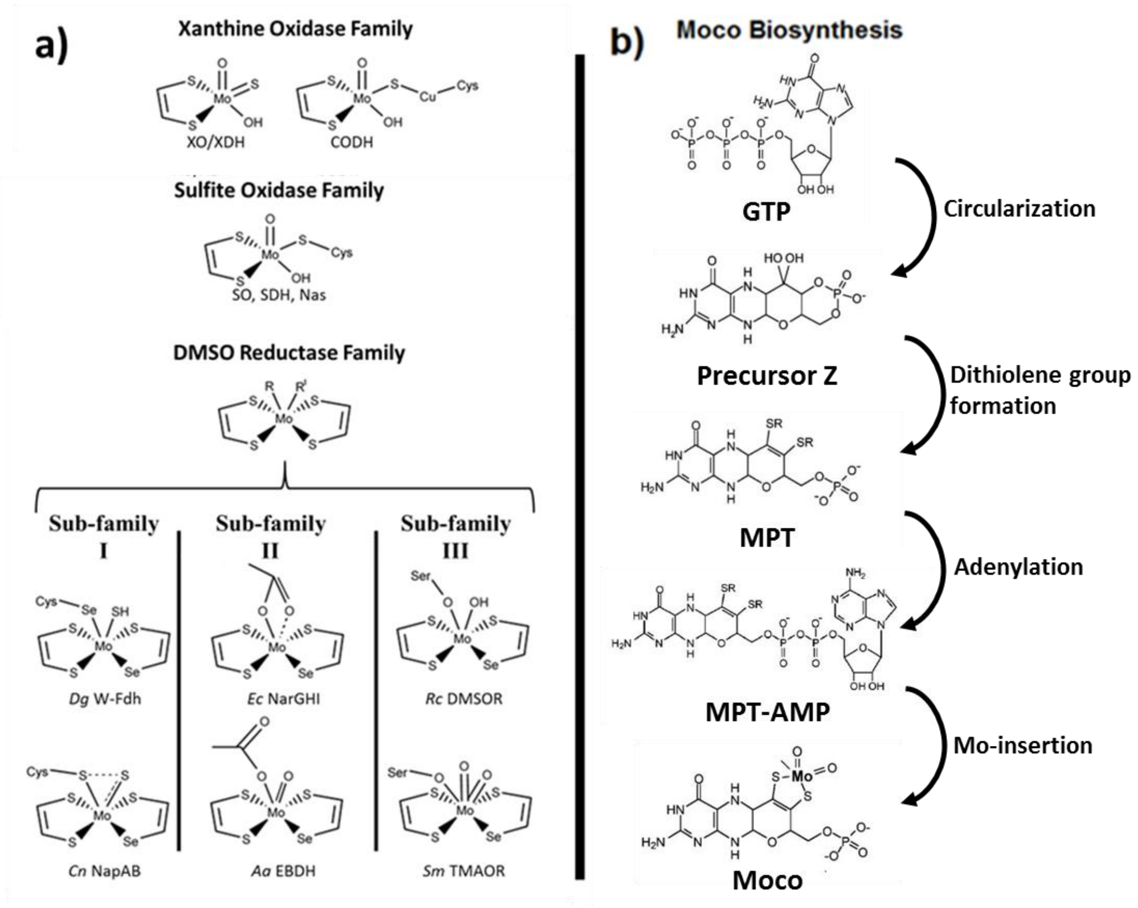
a)
Xanthine Oxidase Family
XO/XDH
CODH
Sulfite Oxidase Family
SO, SDH, Nas
DMSO Reductase Family
Sub-family I
Sub-family II
Sub-family III
Dg W-Fdh
Ec NarGHI
Rc DMSOR
Cn NapAB
Aa EBDH
Sm TMAOR
b)
Moco Biosynthesis
GTP
Circularization
Precursor Z
Dithiolene group formation
MPT
Adenylation
MPT-AMP
Mo-insertion
Moco

**Figure 1.1: Pyranopterin Dependent Enzyme Families and the Moco Biosynthesis.** **a)** Pyranopterin dependent enzyme families and the DMSO reductase sub-families (adapted from Romão 2009 and Coelho & Romão 2015). **b)** Proposal for the eukaryotic Moco biosynthesis (adapted from Mendel 2006). Abbreviations: XO/XDH – Xanthine Oxidase/Dehydrogenase; CODH – CO Dehydrogenase; SO – Sulfite Oxidase; SDH – Sulfite Dehydrogenase; Nas – Assimilatory Nitrate Reductase; Fdh – Formate dehydrogenase; Nar – Membrane bound Respiratory Nitrate Reductase; Nap – Periplasmic Nitrate Reductase; EBDH – Ethylbenzene Dehydrogenase; TMAOR – Trimethylamine Oxide; GTP – Guanosine Triphosphate; MPT – Metal Containing Pterin; AMP – Adenosine Monophosphate.

The pyranopterin is expected to be responsible for the correct positioning of the Mo atom in the catalytic center, to control its redox behavior and to participate in the electron transfer to or from the Mo. The cofactor is found deeply buried within the protein and whenever it is released from the enzyme, it undergoes rapid degradation due to oxidation reactions [3], [5], [6].

The pyranopterin biosynthesis is a conserved pathway that can be divided into four steps (**Figure 1.1.b**) [7]: **I –** Conversion of GTP (Guanosine Triphosphate) into the Precursor Z, the most stable intermediary; **II –** Sulfur transfer to precursor Z, catalyzed by MPT (Metal Containing Pterin) synthase; **III –** MPT adenylation producing the ready to bind Mo (or W) (this process is catalyzed by two proteins in bacteria whereas in higher organisms both were fused into a two-domain protein - Cnx1); **IV –** Mo insertion preceded by a copper atom exit which is thought to preserve the pathway intermediaries from unintended oxidation [3].

In prokaryotes, the pyranopterin is found conjugated to nucleosides whereas in eukaryotes it is in the monophosphate form. Lack of the cofactor synthesis may lead to a decrease or loss of the Moco-enzymes functions in the organism. In humans, it leads to mental retardation and attenuated brain growth followed by death, due to deficiency in SO activity [3], [5].

Note that eukaryotic NR are part of the SO family and are not under the scope of this dissertation.

## 1.2 NITRATE REDUCTASES

### 1.2.1 Biologic and Ecologic Context

Nitrogen is the fourth most abundant element in the biosphere and is the nitrogen cycle that delivers and recycles this essential element throughout the Ecosystem. Nitrogen is involved in many anabolic and catabolic pathways where it can be incorporated into amino acids and nucleic acids or be part of respiration processes. Due to human activities like the overuse of nitrate based fertilizers, the nitrogen cycle “has been altered more than any other basic element cycle” [8].

Nitrate is the most stable and important nitrogen source in soils and water, reduction of nitrate to nitrite - a key step in the nitrogen cycle – becomes therefore important in the management of the ecosystem. This reaction is catalyzed by nitrate reductases (NR) and is the first step in both assimilatory and dissimilatory nitrate reduction pathways [9].

Prokaryotic nitrate reductases belong to the DMSO reductase family of Mo containing enzymes and their functions and localizations vary between nitrogen assimilation (cytoplasmic nitrate reductases - Nas), energy generation (membrane bound nitrate reductases - Nar) and excess energy dissipation (periplasmic nitrate reductase - Nap) [10].

The cytoplasmic assimilatory nitrate reductase (Nas), catalyze the first step of nitrogen assimilation and receive electrons from nicotinamide adenine dinucleotide (NADH), reduced nicotinamide adenine dinucleotide phosphate (NADPH), ferredoxin, or flavodoxin. Respiratory nitrate reductases (Nar) are membrane-bound (facing the cytoplasm) enzymes that obtain the reductive power from periplasmic formate, whose electrons are transferred through the quinone pool to the Nar active site, releasing nitrite into the cytoplasm and contributing to the proton motive force [10], [11].

The true physiological role of periplasmic nitrate reductase (Nap) is not yet fully clear. Periplasmic nitrate reductases are known to be responsible for the redox balancing but they are also involved in the denitrification process, nitrate scavenging and respiration, even though apparently, they do not contribute for the proton motive force. Electrons originating from the quinone pool flow through the tetra-heme monomer NapC, passing by a di-heme monomer NapB, reaching the active site in NapA [10]. The catalytic subunit NapA ranges from 70 kDa (*D. desulfuricans*) to 90 kDa (*C. necator*) and some organisms like *D. desulfuricans* lack the NapB monomer [4], [10].

Nitrate reductases have been implicated in a diverse range of functions, namely denitrification, reduction to ammonia, maintenance of cellular redox potential, nitrate respiration and scavenging. Because these functions are so diverse, knowledge about NR activity in the ecosystems becomes an important step towards the regulation of the nitrogen cycle. Through better understanding these enzymes we can better predict the impact on biodiversity, global warming and water quality – essential problems caused by the gradual disruption of the nitrogen cycle [8], [9].

### 1.2.2 Structure of Periplasmic Nitrate Reductases: State of the Art

The first structure of a NR was solved by X-Ray Crystallography in 1999 ([12]. The protein is a monomer isolated from *Desulfovibrio desulfuricans (Dd)* and the structure was obtained at 1.9 Å resolution. At the time, the model was published with six Mo ligands, four provided by the cofactor cis-dithiolene groups, one from the side chain of a cysteine and the sixth was interpreted as an oxo/hydroxyl ligand. The model showed a distorted trigonal prismatic geometry involving Mo and its ligands [12]. The first crystal structure of a heterodimeric NR (NapAB from *Rhodobacter sphaeroides*) was obtained in 2003 at 3.2 Å resolution [13]. In 2007 the crystal structure of the catalytic subunit NapA from *Escherichia coli* was obtained at 2.5 Å. During purification the NapB monomer would dissociate and therefore its structure was not determined in the study [14].

New crystallographic studies of novel *Dd* NapA structures were later conducted of the protein in the native state and with ligands, with resolutions between 1.99 Å to 2.50 Å. Through improved refinement methods, this work showed that the sixth Mo ligand is a sulfur atom instead of oxygen. The authors also highlighted the proximity between the fifth and sixth ligands, implying a partial disulfide bond. Due to the true nature of the sixth ligand, the initial proposed reaction mechanism (based on oxygen chemistry) needed to be revisited and more research was therefore required [15].

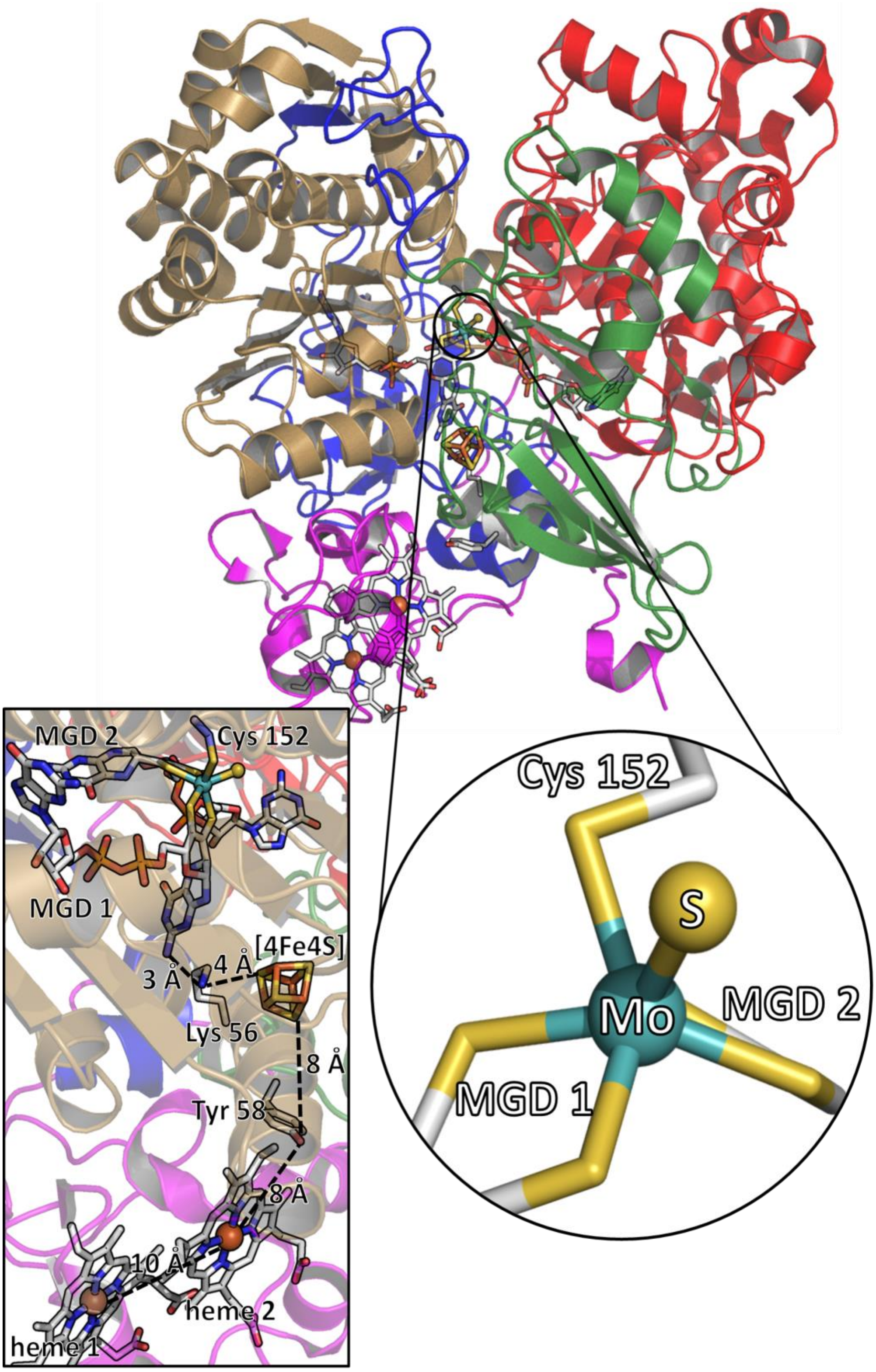
MGD 2
Cys 152
MGD 1
3 Å
4 Å
[4Fe4S]
Lys 56
8 Å
Tyr 58
8 Å
10 Å
heme 2
heme 1
Cys 152
S
Mo
MGD 2
MGD 1

**Figure 1.2: Structure of NapAB from *Cupriavidus necator*.**

The cartoon colors represent the various NapA domains and the NapB monomer: domain I, green; domain II, red; domain III, sand; domain IV, blue; NapB, magenta. A zoom in of the NapAB active site cofactors and electron pathway is shown (rectangle); Zoom in of the active site of NapAB is also shown (circle).

The crystal structure of the heterodimeric NapAB from *Cupriavidus necator (Cn)*, was solved at atomic resolution (1.5 Å) and corroborated that the sixth Mo ligand was a sulfur atom [16]. The authors also published a partially reduced NapAB structure which showed the Mo coordinating cysteine with a novel alternate conformation, further advancing the discussion on the Nap reaction mechanism.

The NapAB from *Cn* is a globular heterodimer of an approximate dimensions of 65 Å x 65 Å x 58 Å and is shown in **Figure 1.2**. The larger subunit, NapA is composed of 802 amino acids and is responsible for catalyzing the reduction of nitrate to nitrite. This monomer contains the Mo atom bound to two molybdopterin guanosine dinucleotide (MGD) cofactors and a [4Fe4S] cluster involved in electron transfer. The active site is buried within the protein, having a 15 Å long substrate channel leading to it in the opposite side of the interface between NapA and NapB. The NapB monomer is responsible of transporting electrons originating from the quinone pool and NapC (a membrane-anchored tetraheme *c-type* of unknown structure), towards NapA. NapB has 134 amino acids and contains two *c-type* hemes – with two histidines coordinating the iron atoms. The electrons reaching the active site originating from the heme groups (10 Å away from each other), are expected to be mediated by the conserved NapA tyrosine 58 (8 Å away) that is at the interface between NapA and NapB and reaching the [4Fe4S] cluster (also 8 Å away). From the [4Fe4S] cluster, the electrons should first pass through the highly conserved NapA lysine 56 (4 Å away) and finally reach the nearest MGD cofactor that is 3 Å away. The NapA from *Cn* is organized in 4 domains: I – residues 4–68, 507–531, and 600–641; II – residues 69–148, 386–506, and 532–599; III residues 149–385; and IV residues 642–802. The N-terminal domain (I) contains the four cysteine residues coordinating the [4Fe4S] cluster, domains II and III have an overall similar α/β fold and each one binds one of the two MGD cofactors. The domain IV is a β-barrel and is very exposed to the solvent.

### 1.2.3 Proposed reaction mechanism and its considerations

Based on the Mo chemistry and the nature of the sixth ligand, three alternative reaction mechanisms where initially proposed [15], [17], [18]. These hypotheses can be differentiated by the combination of two aspects – substrate direct/indirect binding to Mo and preservation/breaking of the Mo-fifth ligand: (**Figure 1.3.a**) Substrate direct binding to Mo and breaking of the bond between Mo and its fifth ligand; (**Figure 1.3.b**) Substrate second-sphere coordination to the Mo ligand; (**Figure 1.3.c**) Substrate direct binding to Mo. [17]–[21]

The proposed reaction mechanism also states that the formation of bonds and/or partial bonds between the fifth and the sixth sulfur ligands plays a role in the redox state of molybdenum. This is corroborated by the different crystal structures where the distances vary between 2.17 Å and 2.80 Å – where the van der Waals contact distance is 3.3 Å [4], [15].

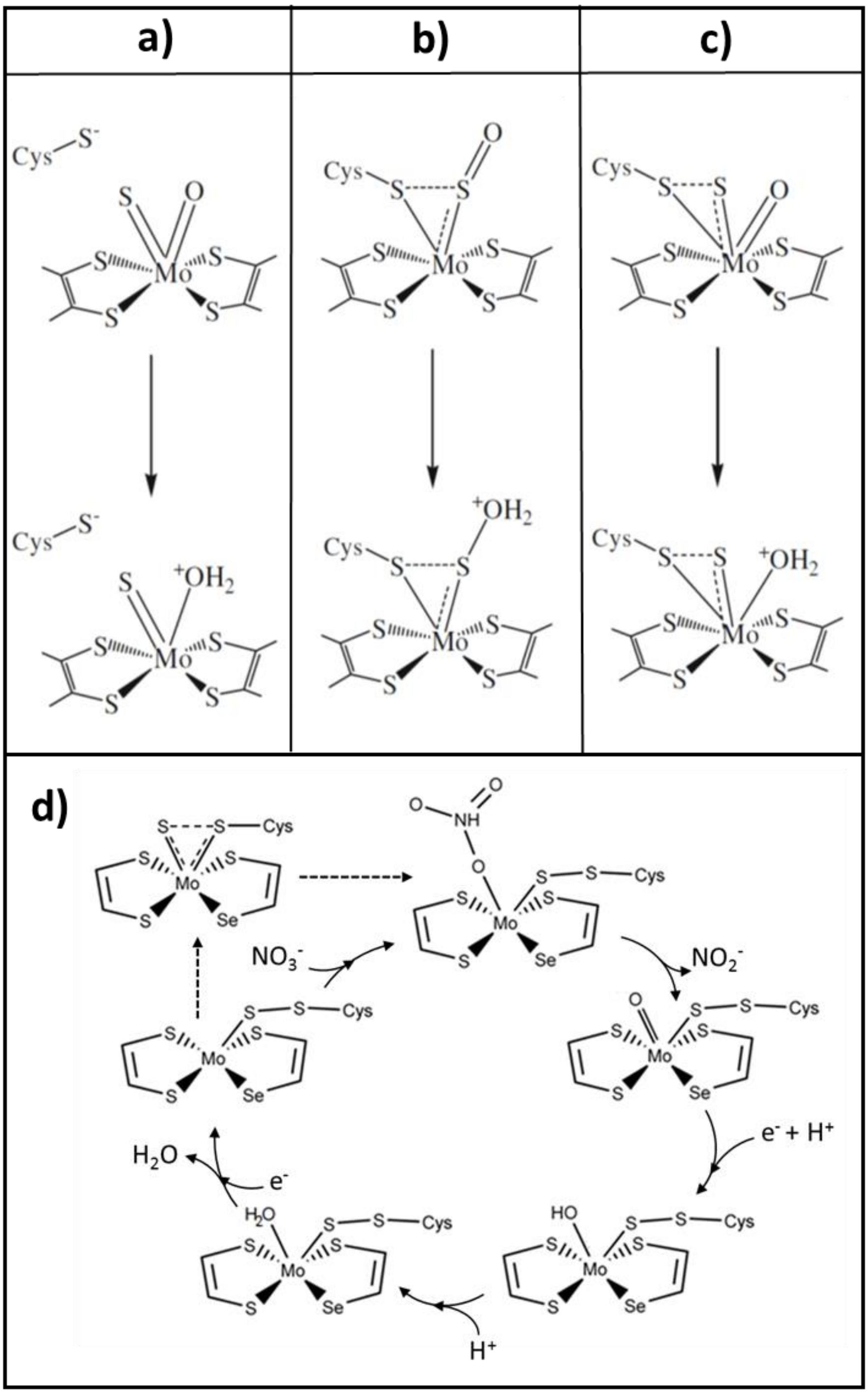

**Figure 1.3: NapAB proposed reaction mechanism.**
**a-c** (adapted from Najmudin *et al.*, 2008): the various considered possibilities for the substrate interaction with the active site. **a**) Substrate direct binding to Mo and breaking of the bond between Mo and its fifth ligand; **b**) Substrate second-sphere coordination to the Mo ligand; **c**) Substrate direct binding to Mo. **d)** the proposed reaction mechanism for Nap [17]–[21].

Independent studies involving computational chemistry were also performed. In all cases the authors concluded that a first coordination sphere mechanism where the cysteine remained indirectly bound to the Mo atom was energetically more favorable [17], [18].

The proposed mechanism implies that for the enzyme to become active, a conformational rearrangement must first occur (**Figure 1.3.d**). This rearrangement involves the Mo coordinating cysteine changing from a first coordination shell to a second coordination shell ligand. The cysteine's side chain loses its Mo bond and starts bonding to the sixth ligand, which in turn shifts towards the fifth ligand's prior position. From this rearrangement originates a free Mo coordinating position where the substrate may bind [4], [22]. After substrate binding, catalysis follows and an oxygen atom is left bonded to Mo. For the active site regeneration two electrons and protons are transferred to the remaining oxygen and a water molecule is released. The catalytic cycle continues until nitrate is consumed and the inverse of the sulfur shift occurs.

A partially reduced NapAB structure from *Cn* was obtained at 1.7 Å resolution [16]. During refinement of this structure, the Mo coordinating cysteine (Cys 152) presented extra positive electron density near the $C_\beta$. The authors interpreted this new density as a cysteine alternate conformation with 12% occupancy. The mechanism hypothesis previously described is corroborated by this structure. The conformational freedom of the active site, the bond and/or partial bond interaction of the fifth and the sixth sulfur ligands with the subsequent computational chemistry studies sustains the proposed mechanism. However further studies are necessary to establish the NR reaction mechanism [17]–[21].

## 1.3 X-RAY CRYSTALLOGRAPHY

Macromolecular X-Ray Crystallography is a technique used to solve the 3-D macromolecular structures up to atomic resolution. This technique takes advantage of the crystal high degree of organization and the X-ray characteristics – the wavelength range compatibility to the atomic bonds and the diffraction pattern of the electrons [23].

This technique is used worldwide and its major drawback are the difficulties in obtaining crystals. X-Ray Crystallography was the first technique to deliver atomic resolution structures and is until today the most used technique for such purposes. By August 2017, the protein data bank (https://www.rcsb.org/pdb/statistics/holdings.do) holded 132428 structures from which 118533 (90 %) were provide by X-Ray Crystallography. Other available structural biology techniques are Nuclear Magnetic Resonance (NMR), Cryo-Electron Microscopy (Cryo-EM) and Small-angle X-ray scattering (SAXS) that possess different sets of advantages/drawbacks. X-Ray Crystallography, NMR and Cryo-EM can be used in separate to produce detailed 3-D structures or may also be combined, complementing each other to succeed in particular cases.

### 1.3.1 Protein crystallization

The crystallization of proteins is a procedure which relies on diverse ways of gradually increasing the protein concentration. The event must be slow and gentle enough so that the proteins precipitate in an organized manner, leading to the formation of crystals. Crystals are highly organized matter and can be represented by the unit cell – the smallest group of molecules that can reconstruct the crystal by symmetry operations. Unit cells are characterized by the length of “a”, ”b”, and ”c” and the “α”, “β” and “γ” angles between them [23]. Unit cells contain at least one asymmetric unit, which reconstructs the unit cell by symmetry operations and belong to one of four types: Primitive lattice (P), base-centered lattice (A, B or C), internal-centered lattice (I) or face-centered lattice (F). When combined with the seven crystalline systems, 28 crystalline lattices are available. Since proteins are chiral, the symmetry operations available are translation and rotation, excluding any mirror planes or inversion centers. Because of this, the possible space groups for protein crystals are reduced from 230 to 65, all of them available for consult at “*The International Tables for Crystallography”*. Protein crystals contain water channels which represent 30-70% of the crystal as first described by Matthews [23], [24]

Protein crystals are used to diffract X-rays. Planes of atoms within the crystals act as X-Ray reflectors through constructive interferences serving as signal amplifiers. The diffraction of unorganized atoms within the crystal will cause destructive interference, whereas diffraction from the organized atoms will be recorded in the diffraction patterns [23].

#### *1.3.1.1 Phase Diagrams and the Crystallization Process*

Phase diagrams may be composed of various zones, namely precipitation, nucleation and crystal growth and represents the crystallization process for each unique protein (**Figure 1.4**). For maximizing the probability of obtaining adequate crystals, the crystallographer attempts to obtain a solution that conveniently passes through the three stages in. The objective is to start in the unsaturated zone (**Figure 1.4.a**). As water moves out of the crystallization droplet, the protein and the precipitants concentration increases because the water volume is reduced. In theory, as the protein and precipitant concentration arise, the crystallization droplet changes

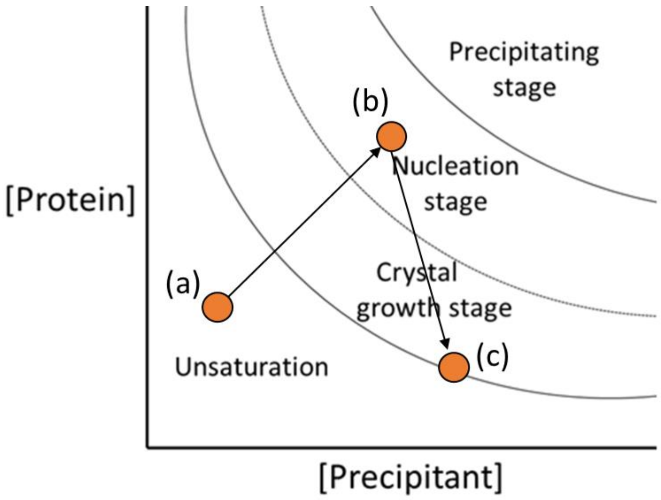

**Figure 1.4: A protein crystallization phase diagram.**
In the diagram is shown a hypothetical crystallization condition progress along time (brown circles). The protein droplet passes by the crystal growth zone (**a-b**) reaching the nucleation zone (**b**). Here crystal nucleus are generated and start to grow, lowering the dissolved protein concentration. The droplet leaves the nucleation zone, passing the remaining time in the crystal growth zone. The crystals grow until no more protein is available, hence reaching the interface between the crystal growth and unsaturation zone (**c**).

from the unsaturated stage, to the nucleation stage (**Figure 1.4.b**). The droplet passes by the crystal growth stage because here it cannot form new nuclei and there are not existing nuclei to grow. When the nucleation stage is reached, the protein begins to form crystal nuclei, so its concentration starts to decrease. As the protein concentration lowers, the droplet changes towards the crystal growth stage again (**Figure 1.4.c**). When this stage is achieved, the already formed nuclei continue to grow, forming crystals. The crystals will grow until the solution reaches equilibrium or is perturbed [23], [25].

This is a complex and not yet fully understood phenomenon, often needing fine-tuning of key conditions. Because of this, and the fact that so many (non-exhaustively testable) conditions vary on significance for each protein to be crystallized, the crystallization step is still partially empiric [23].

#### *1.3.1.2 Crystallization Methods*

There are several crystallization methods, ant the most common is the vapor diffusion method, which can be performed by the hanging or sitting drop techniques. In hanging drop, the crystallization condition containing the precipitating agent is applied on the top of a silanized cover slip and the protein is added, followed by sealing of the well with the cover slip. Since there is a lower precipitant concentration in the drop, water slowly diffuses into the reservoir. In the sitting drop method the drop containing the precipitant/protein is placed in a small platform inside the well (**Figure 1.5**) [23].

Other methods used in protein crystallography are dialysis and micro batch. The first consists in a small button enveloped by a dialysis membrane and immersed in the crystallization condition. The dialysis button has a depression where the protein is previously added, therefore, protein-crystallization solution contacts are made only through the dialysis membrane. The micro batch is a technique that makes use the protein and water insolubility in oil. In this technique, the protein and crystallization solution are added to oil in the bottom of the well as a single drop. Water will migrate from the drop to the oil at an even slower rate than for instance, vapor diffusion [23].

The use of crystallization robots for automated crystallization is a popular and appealing option. Crystallization robots are used for initial screening assays. Using special crystallization plates, the robots automatically add the protein and crystallization solutions to the wells. The machines complete the screening assays much faster, but also use significantly less protein amounts (down to the nano-scale) that humans are able to. The major downfalls of the robots is that the crystals are usually smaller and a scale up is required, which might be complex and problematic in specific cases [23], [26].

#### *1.3.1.3 Co-crystallization, Soakings and Cryoprotectant Solutions*

Proteins in the crystalline form may retain their function and tolerate some conformational changes induced by ligands without damaging the crystal [23], [25], [27]. Besides structures of site-specific ligand interaction with the proteins, important

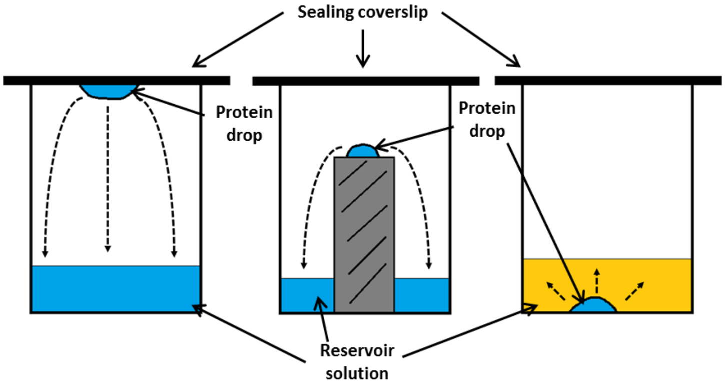

**Figure 1.5: Representations of the principle vapor diffusion method techniques: hanging drop, sitting drop and microbatch.**
A simple representation of the three crystallization methods used in this work. The dashed arrows represent the movement of water from the protein drop to the reservoir. a) Hanging drop; b) sitting drop; c) microbatch.

conformational changes caused by the ligands can be revealed. For this purpose, several procedures such as co-crystallization or soakings experiments can be made.

Co-crystallization consists in crystallizing the protein while the ligand is dissolved in the crystallization drop, either by previously incubating the protein with the ligand, or by adding the ligand to the protein drop during the crystallization. Soaking experiments consists in introducing new solutions that contain the ligand in pre-existing crystals. The ligand diffuses through the water channels within the crystal and interact with the protein molecules. If drastic conformational changes are expected, co-crystallization might be preferable to avoid crystal damage.

After the crystals are grown, they can be transferred to stabilizing and cryoprotectant solutions for diffraction experiments. In order to prevent the crystals from dissolving, the solutions used possess higher precipitating agent concentrations than in the conditions that they grew. During the diffraction experiments or transport, liquid nitrogen (-197 ˚C boiling temperature) is used. Aiming to avoid the water within the crystals to freeze and damage them, cryoprotectant solutions are used. The cryoprotectant solutions possess a cryoprotectant agent that inhibits the formation of water crystals. For these purposes glycerol, xylitol, sugars, Polyethylene Glycol (PEG), salts or mixtures of these are used [23].

### 1.3.2 X-Ray Sources

The first generation of X-Ray sources were the X-Ray tubes, in which electrons collided with an anode under vacuum conditions. In these conditions, when the electrons hit the metal, inner orbital electrons are ejected from it. An outer orbital electron then fills the empty orbital and releases energy in the form of X-rays. Each metal emits photons in varying specific wavelengths. However, this procedure heavily degrades the metal in the zone that the electrons collide. To solve this problem, other X-Ray sources were invented – the rotating anode X-Ray tubes. In this case the anode was rotating and the area of impact of electrons was distributed along the anode. By doing this, the degradation of the anode was dispersed in a larger area. Although, the temperature rise under vacuum conditions did remain a problem [23].

Synchrotron radiation is widely used nowadays. Electrons are accelerated in storage rings to near the speed of light and emit X-Ray photons when forced to change in direction but continue to accelerate. The photons released pass through monochromators that make X-Ray wavelength selection possible. Synchrotron radiation further revolutionized X-Ray crystallography in the drastic time reduction required for data collection, data quality and crystal size requirement [23].

A more recent X-Ray source is the Free Electron Laser X-Ray (XFEL), where the electrons are instead accelerated in a straight line. This technology produces extremely brilliant and short pulses. Because of this, data can be collected free of radiation damage – the radiation pulse exits the sample faster than the damage occurs [28].

### 1.3.3 Protein crystal diffraction

In the diffraction experiment X-rays go through a protein crystal and are diffracted by the electrons of the protein. The diffracted beams hit the detector and its intensities and relative positions are recorded. Although the phase information is not detectable and therefore lost. The experiment results in a diffraction pattern, a plane with various spots varying in size proportionally to photon count. The crystal orientation is changed over the course of the diffraction experiment, obtaining thousands of diffraction patterns, reflected from the different lattice planes of the crystal. The diffraction patterns are indexed forming a hypothetical 3D diffraction pattern sphere (**Figure 1.6.a**). The result of the experiment is a list of intensities across the reciprocal space sphere and correspondent errors [23].

Since the crystal is a periodic organization of molecules, some atoms diffract in the same direction and in phase with each other in all the unit cells which constitute the crystal. These atoms are said to diffract X-rays in a constructive manner, increasing its signal proportionally to the number of such atoms. In contrast atoms not structurally repetitive inside the crystal (as for solvent channel's waters) give diffractions varying in direction and phase that cancel each other [23]. W.H. Bragg and his son W. L. Bragg discovered and mathematically described this phenomenon now known as the Bragg's Law (**Figure 1.6.b**).

The planes of atoms within a crystal that produce constructive diffraction can be represented by three numbers, called the Miller indices (or lattice indices) – *h,k* and *l*. These indices represent sets of parallel planes with constant interplanar spaces of $d_{hkl}$. If the scattered waves from X-rays are in phase, they interfere constructively. When these conditions are met, constructive interference happens, resulting in multiple diffracted/reflected X-rays in the same direction and in phase – a strong diffracted beam that produces a spot in the diffraction pattern. Each crystal orientation has a different number of sets of planes that meet the Bragg's law condition. The crystal is rotated in order to capture the diffraction of more planes of atoms [23].

For diffraction data evaluation, various parameters are used in combination. Some of the more used parameters and its expected values are: Ratio of signal to noise ($I/\sigma(I)$) (should be no less than 2); completeness, which represents the percentage of measured expected reflections (should be above 95% at the highest resolution shell); 3); correlation coefficient ($CC_{1/2}$) representing the correlation between two halves of a randomly split data

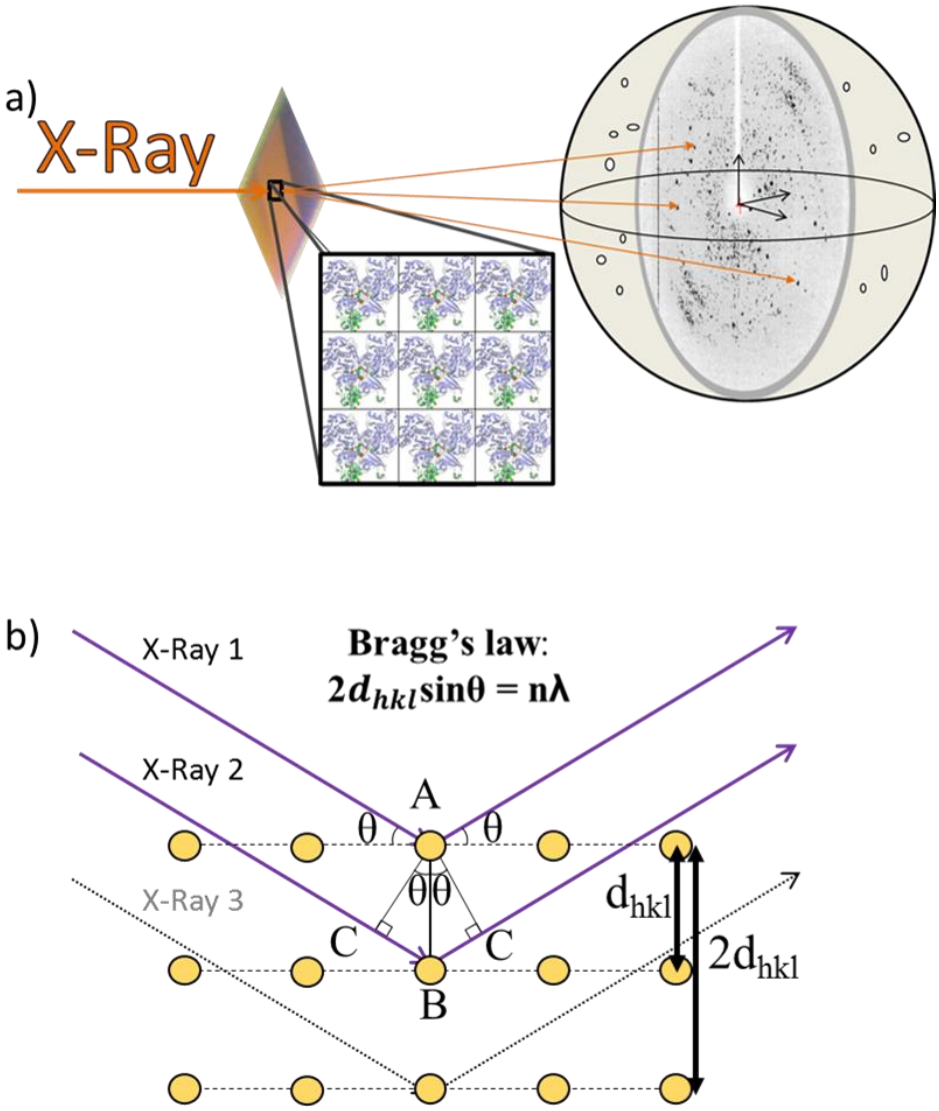

**Figure 1.6: Schematic representation of the diffraction experiment and constructive interference.**
**a)** X-rays go through a Nap crystal which results on a diffraction pattern. As the crystal rotates more diffraction patterns are collected that forms a hypothetical reciprocal diffraction sphere. Symbolizing the unit cells are Nap structures. The crystal photo, diffraction pattern and NapAB structures have all been experimentally obtained during the course of this work. **b)** Constructive interference is produced from sets of planes (horizontal dashed lines) of atoms (yellow dots), with interplanar spaces of $d_{hkl}$, from impinging X-rays of wavelength λ with a θ angle only if Bragg's law is met. To the right a simple description of the relation between interplanar spacing and difference in path length of X-Rays 1 and 2 (adapted from Rhodes 2007).

set (should be no less than 0.5); 4); and $R_{merge}$ which is the averaging of multiple symmetry-related reflections, depending on the study case a value lower than 0.25 is acceptable [23].

### 1.3.4 The Phase problem

Fourier showed that any complex periodic function can be described as the sum of simpler periodic functions. Diffracted X-rays can be described as threedimensional waves, they are therefore a complex periodic function and can be described as the sum of various simpler functions [23].

The 3D electronic distribution of the atoms in the protein can be calculated using the Fourier Transform (FT). The FT transforms the values of a periodic function in their reciprocal values, in the case of X-Ray Crystallography it transforms the reflection data (reciprocal space) into electron density data (real space). FT is reversible, therefore applying it to electron density data gives back the reflection data [23].

The FT requires the amplitudes and phase angles to transform diffraction data into real space information. Amplitudes are calculated directly from the indexed list of reflection intensities experimentally obtained. The phase angles are however missing, resulting in the "phase problem" where the crystallographer needs to obtain phase information by other means [23]. Molecular replacement is one way of obtaining phase information. It is popular and widely used because it does not require any additional experiments, but does require an already existing homology model of the protein in study. The method consists in placing the already obtained structure into the new unit cell. After translation and rotational operations, the phases of the X-rays this structure would diffract are calculated. These phases are taken as initial estimations of the real unattained phases [23], [25].

### 1.3.5 Model Improvement

With the estimated phases and the measured intensities, the FT is applied and a 3D description of the protein electronic distribution is obtained. This model is however greatly influenced by the model used in Molecular Replacement procedure, in fact the phase information dominates the amplitude information [23].

The crystallographer interprets the electronic density and makes adjustments that in principle will approximate the model to the real structure. After significant adjustments are made, another FT is practiced resulting in reciprocal-space information about the structure, therefore amplitudes and phases. Mathematical analysis are made, further progressing phases, approximating the model's calculated structure factors to the experimentally obtained. Cycles of FT and model improvement are made, converging the 3-D model to the structure that experimentally diffracted the X-Rays [23], [25], [27].

### 1.3.6 Model analysis and validation

During model refinement, various parameters are used to evaluate how close it is to the obtained data and how much more it can be improved, such as different electron density maps, temperature factor, R-factors and the Ramachandran plot.

During model building the atoms are fitted into the electron density where there is enough confidence to do so. Common contour maps used are $2F_O\text{-}F_{calc}$ and $F_O\text{-}F_{calc}$. The $2F_O\text{-}F_{calc}$ map results in continuous density along the model, giving increased importance to observed structure factors over the calculated ones. The $F_O\text{-}F_{calc}$ map is a difference map that shows negative or positive density. Positive density represents lack of electron density compared to what obtained data suggests, whereas negative density is the inverse. This map can show subtler errors that the $2F_O\text{-}F_{calc}$ [23].

The temperature factor (B factor) represents the thermal vibration expected for each atom in the model and is expected to be lower for atoms buried inside the protein and higher for atoms at the proteins surface. The thermal motion of each atom is expected to be similar to neighbor atoms and higher for side chain than the protein's backbone [23], [25], [27].

Other parameter used for model analysis and validation is the R-factor - a measure of the proximity between the current model and the experimentally obtained data. If during refinement the model is converging to the real 3D structure, this factor will converge also to 0. There are diverse ways to calculate R-factors, the "traditional" R-factor is given by:

$$R = \frac{\sum ||F_{obs}| - |F_{calc}||}{\sum |F_{obs}|}$$

If the model would be perfectly equal to the structure that diffracted the X-rays R will be zero, whereas if $F_{calc}$ are random values from another dataset R will be 0.6 or higher. The $R_{free}$ is an R-factor that uses a random set of data not used in refinement (usually 5 %). The two factors complement each other in what the "traditional" R-factor tells us how well the current model predicts the obtained data and $R_{free}$ how well the current model is predicted by data not used to arrive to the same model [23], [25].

Another way to evaluate a model is to stereochemically compare it to the amino acid conformations in the Ramachandran plot. These plots represent preferable and allowed amino acid conformations since they are physically restricted. It is allowed that a few outliers remain through refinement but not too many. These amino acids remain outliers because they are tolerating a higher energetic cost in order to maintain the protein's function.

## 1.4 ISOTHERMAL TITRATION CALORIMETRY (ITC)

Isothermal titration calorimetry (ITC) is a very powerful technique and the objective of using ITC was to try to obtain the kinetic constants for *Cn* NapAB and its interaction constants with various ligands, further characterizing it.

The ITC machine contains two isotermically isolated compartments (the reference and the reaction cell). By altering the energy provided to the reaction cell, the machine maintains the temperature of both cells constantly equal. The result of the experiment, is the variation of energy provided to the reaction cell along time. Exothermic reactions occurring inside the reaction cell lead to a decrease in energy provided to the reaction cell, maintaining the temperature; whereas endothermic reactions lead to an increase of energy providence [29], [30].

The process of determining reaction kinetics through ITC generally requires two steps: the first is the acquisition of the total apparent molar enthalpy ($\Delta H_{app}$) in the established conditions, the second is the measurement of the heat flow at different substrate concentrations [29]. For determining $\Delta H_{app}$ a single injection experiment is performed in which the substrate injected is totally converted into product. Because the substrate is totally consumed, it is assumed that the moles of product obtained are proportional to the moles of substrate injected; therefore, enabling to calculate the reaction total apparent molar enthalpy [29], [30]. After $\Delta H_{app}$ has been calculated, the heat flow ($dQ/dt$) for different substrate concentrations is needed. To do this there are currently two methods available, the multiple injection and the single injection methods [29], [30].

$$v = \frac{d[P]}{dt} = \frac{1}{V.\Delta H_{app}} . \frac{\mathrm{dQ}}{dt}$$

The multiple injection method involves consistent injections of substrate into the cell containing the sample. Each injection is timed to permit the signal to stabilize to the new baseline but not for the substrate to be significantly consumed – simulating steady state conditions. In this method, the heat flow is calculated through the difference between the original baseline and the new after each injection. In the single injection, the method of calculating the enthalpy of the reaction is similar but requires higher substrate concentrations. Comparing the two methods, the single injection requires more complex mathematical analysis, takes less experimental time and is more resilient to base line drift derivate errors [29], [30].

## 1.5 THERMAL SHIFT ASSAY (TSA)

The thermal shift assay technique (TSA) has become very important, since it is a simple and fast technique able to screen various buffers and/or ligands detecting their influence in the protein of study. This is especially useful for macromolecular X-Ray Crystallography in order to discover stabilizing buffer conditions suitable for the crystallization assays [31]–[33]. In the TSA assays, a fluorophore that improves its emission efficiency when interacting with hydrophobic residues of the protein is used to monitor protein denaturation. As the temperature rises and the proteins start to denaturate, the fluorescence increases its emission and is detected in a RT-PCR machine. The melting temperature ($T_m$) – which is the temperature at which half the proteins is denatured – is measured for the native protein and for the protein in the presence of several ligands of interest and/or buffers [33].

When a ligand stabilizes the protein, the $T_m$ increases and when the ligand destabilizes the protein, the $T_m$ decreases. An inhibitor that interacts exclusively with the folded protein active site is an example of a stabilizing ligand, whereas a ligand that interacts exclusively to the unfolded protein will destabilize it. Ligands that stabilize the protein in these assays, often also improve the macromolecular crystallization process [33], [34].

The result of the technique is a melting profile for each compound tested with the protein and the corresponding melting temperature. The influence of each ligand is accessed through the comparison of melting profiles with the profile absent of any ligand [35].

## 1.6 MICROSCALE THERMOPHORESIS (MST)

Microscale thermophoresis (MST) is a relatively recent technique and it basically consists in the measurement of local loss of fluorescence after heating. The sample consists of at least one labeled analyte, (usually a protein labeled with a fluorophore), producing fluorescence and a ligand. Multiple capillaries containing the analyte and varying ligand concentrations are introduced into the MST machine. The machine is constantly measuring the emission of the fluorophore. At a certain point, it irradiates the center of the capillary with infrared heating. Normally the fluorescence will decay as the molecules will flow from the heated part of solution to the coolest, (the inverse, although less common, might also happen). In either case a signal profile is created depending on the quantity and velocity at which the molecules diffuses away (or into) the heated volume [36].

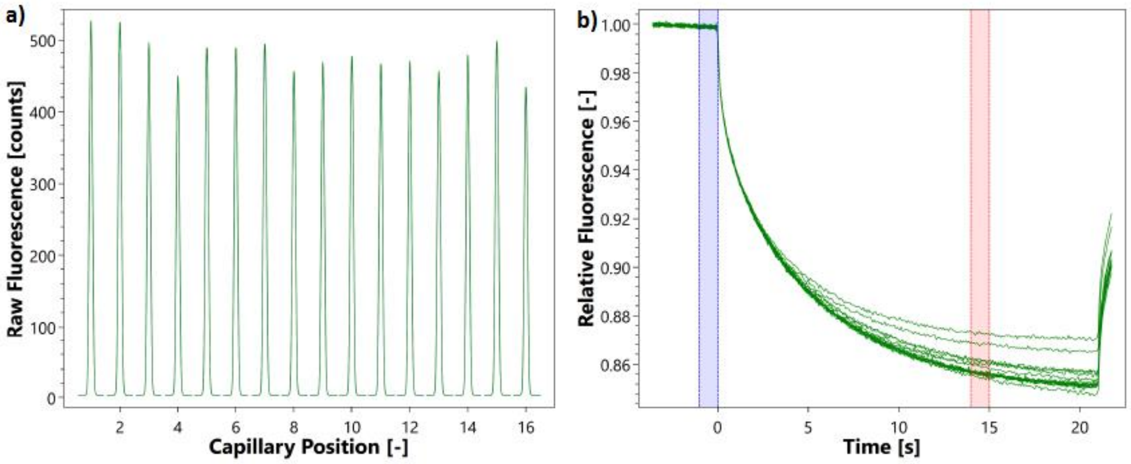

**Figure 1.7: Typical MST experimental results.**
**a)** superimposed capillary scans before and after the MST tracing. **b)** MST traces where the blue and red areas are the non-irradiated fluorescence and irradiated values that are being considered for the $K_d$ calculations.

As each capillary contains increasing concentration of ligand, if it interacts to the analyte it will often change the signal profile. The signal change depends on the difference in size, charge and hydration shell of the protein and protein-ligand complex. From the gradual change in signal dependent on the ligand concentration, the $K_d$ can be obtained. The normal experiment consists on a capillary scan before and after the MST traces (**Figure 1.7.a-b**). These scans assess if the protein is stable enough before and throughout the experiment. Between these scans the MST tracing experiment is performed. This tracing consists measuring the fluorescence without impinging infrared light for a brief period of time (usually for 20 seconds). After this step, the infrared is turned on and the varying fluorescence is measured along time, following the fluorophore diffusion. The signal stabilizes after some time, at which point the velocity of diffusing molecules away and into the irradiated zone is the same. The infra-red is turned off again and the signal rapidly stabilizes to the initial signal. A comparative study is made with the non (infrared) irradiated fluorescence and the irradiated fluorescence [36].

## 1.7 OBJECTIVES

The aim of this work was to study the reaction mechanism of the periplasmic nitrate reductase (NapAB) from *Cupriavidus necator* through the use of X-Ray Crystallography and complementary techniques. To try to obtain the reaction mechanism intermediates various co-crystallization and soaking experiments were conducted using substrate, substrate-analogues, inhibitors and reducing agents.

Besides the X-Ray Crystallography studies, Isothermal Titration Calorimetry (ITC), Thermal Shift Assays (TSA) and Microscale Thermophoresis (MST) were also performed.

These techniques were used because they can provide complementary information on ligand-protein interactions, valuable for the study of the reaction mechanism.

# 2 MATERIALS AND METHODS

## 2.1 PROTEIN PURIFICATION

The *Cupriavidus necator (Cn)* NapAB protein used in this work resulted from a homologous expression system, with the particularity that all the genetic engineering steps were carried out in *Escherichia coli* and later the resulting vector was introduced in an inactive strain of *C. necator*. An industrial growth of 300 L was carried out to obtain large amounts of the bacteria *C. necator* and after pellet resuspension the periplasm was isolated and frozen at -80°C in aliquots of ~1L until further usage [26].

In this work, the purification steps started from one of this periplasm aliquots. The sample was thawed in an ice-water bath, centrifuged at 13000 g for 20 min and the supernatant was dialyzed in 10 mM MES pH 5.5 overnight. The dialyzed solution was centrifuged at 13000 g for 15 min and the resulting sample was always maintained at 4˚C further on. To purify the protein the resulting supernatant was injected in a HPLC (High Performance Liquid Chromatography) system (Shimadzu) connected to a cation exchange SP Sepharose Fast Flow column (GE Healthcare) pre-equilibrated with 10 mM MES pH 5.5. A linear gradient of 10 mM MES pH 5.5 with 500 mM NaCl was used for NapAB elution. The initial flux of the column was 3 mL/min but due to technical problems the flux was lowered to 0.35 mL/min (overnight) and finally to 1.5 mL/min. Continuous absorbance at 280 nm was recorded to follow protein elution and 15 aliquots of 3 ml were collected. To verify which of the collected fractions contained the NapAB protein, an SDS – PAGE (Sodium dodecyl sulfate – Polyacrylamide gel electrophoresis) was used. Samples of 15 µL were previously denatured and loaded into 13% acrylamide Tris-Tricine gels. An electric field of 200 mA and 200 V was applied for 50 minutes and the NZY Color Protein Marker II (NZY Tech) was used to identify the resulting bands.

The fractions containing NapAB, were pooled together and concentrated using a Macrosep concentrator (30 kDa, Pall corporation) and later injected into a molecular exclusion Superdex 200 (GE Healthcare) HPLC column. The column was pre-equilibrated with 300 mM Tris-HCl pH 7.6 and three separate runs were performed at 1 ml/min flow collecting 1 mL aliquots. A SDS-PAGE following the previously described protocol was used to verify which collected samples contained the NapAB protein and the corresponding fractions were pooled together.

Protein purity and concentration where assessed through SDS-PAGE and absorbance at 410 nm which corresponds to the two *c-type* heme groups ($\varepsilon = 212\ 000$ $M^{-1}$ $cm^{-1}$) from NapAB. The final NapAB concentration was 16.9 mg/mL (158 µM) with a purity ratio ($A_{410nm}/A_{280nm}$) of 95%, also confirmed by using a plate reader).

Qualitative activity assays were made to ensure the purified NapAB sample was active. We used sulfanilamide and N-1-napthylethylenediamine dihydrochloride (NED) under acidic conditions to detect the presence of nitrite in various samples. This reaction was first described by Griess in 1879, hence the reaction mixture can be abbreviated to the "Griess reagent" [37], [38]. Each sample solution had a total of 500 µL and was (prior to the addition of the Griess reagents) 100mM Tris-HCl pH 7.6, 1 mM methyl viologen, 4 µM NapAB and 9.2 mM sodium dithionite. After one minute, potassium nitrate was added to a concentration of 14 mM and the reaction was allowed to proceed for half a minute after which the sample was vortexed, oxidizing dithionite and stopping the reaction. A volume of 500 µL 35 mM sulfanilamide and 6 M HCl was added to the sample mixture followed by 500 µL 5 mM NED. The development of an intense pink color was then assessed.

## 2.2 PROTEIN CRYSTALLIZATION

### 2.2.1 Screening and optimization

Crystallization assays where performed in a temperature controlled room at 20°C and all the necessary material was there placed for at least 30 min prior to the beginning, including the 24 well-plates used (Molecular Dimensions - XRL).

Considering the previous successful C.*necator* NapAB crystallization studies [16], [26], two crystallization conditions were initially tested by the hanging drop method using 100 mM Bis-Tris pH 5.5 and 100 mM succinic acid pH 7.0 with 5% to 30% PEG 3350. Different NapAB initial concentrations were also tested: 17 mg/ml, 12.75 mg/ml and 8.5mg/ml. The drops contained 1µL of protein solution and 1µL of precipitating solution (1+1) and 500 µL of crystallization solution in the reservoir. In parallel, an additive screen from Hampton Research (total of 48 different additives) was also tested by hanging drop using the crystallization condition of 0.1 M succinic acid pH 7.0, 20% PEG 3350 and drops composed by (1+0.25+0.75) of protein, additive and precipitant solution respectively. To clarify the crystallization drop composition, in all cases the pipetting order was: protein sample on a silanized cover slip or crystallization bridge; additive solution (when applied) on top of the protein drop; and precipitating solution followed by the sealing of the well.

The commercial screen JCSG-plus™ from Molecular Dimensions (96 different crystallization conditions) was also tested using the hanging drop method and drops (1+1) in the search for alternative crystallization conditions. The JCSG$^{+}$ screen results showed that 9 out of 28 initially promising conditions were worth to pursuit and were reproduced using in-house made solutions. From these nine conditions, the condition containing 0.1 M ammonium citrate pH 5.5 with 20% PEG 3000 was selected and PEG concentrations of 15%, 20%, 25% and 30 % were also screened. The condition containing 20% PEG 3000 was originally chosen, however, co-crystallization of NapAB with reducing agents caused a decrease of the crystals size and an increase of the presence of smaller crystals. Due to this, we retested PEG 3000 for 15%, 17.5%, 20% and 22.5% and the condition containing 17.5% PEG 3000, 0.1M ammonium citrate pH5.5 proved to lead to better crystals and chosen as the main crystallization condition until the end of this work.

### 2.2.2 Co-crystallizations and soakings

Two main crystallization methods were used in order to try to obtain the NapAB crystals with ligands: co-crystallization and soaking. Co-crystallization was used either by incubating Nap with the ligands for 30 min prior to the crystallization assay or by adding the ligand to the crystallization drop as an additive. Soaking experiments were carried out either by fishing the crystals into a new drop containing a harvesting solution (HB) with the ligand or by exchanging the drop by successively and gently substituting the mother liquid by the HB/ligand solution.

Potassium nitrate (1 0 mM or 100 mM) and sodium nitrate (10 mM) were tested to verify if the salts were relevant as additives using drop volumes of (1+0.5+0.5) and (1.5+0.5+1). Co-crystallization with reducing agents (DTT and TCEP at 14 mM) by incubation with NapAB was also tested using hanging drop (1+1; 1.5+1.5; 2+2), sitting drop (1+1) and the micro batch (2+2) techniques. For incubation assays the final concentration of the reducing agent was 14 mM and the NapAB sample concentration was 13.6 mg/ml. The incubation periods lasted 30 minutes for all cases.

The incubation of Nap with reducing agents resulted in a low yield of large protein crystals, favoring the appearance of smaller crystals in high amounts. To improve crystal size of NapAB with reducing agents, we tested: (**1**) different Nap concentrations (158 µM, 126 µM, 111 µM and 79 µM); (**2**) different drop volumes (1+1; 1.5+1.5 and 2+2); (**3**) decreased crystallization temperature at 4 $^0$C; (**4**) urea and potassium nitrate as additives, through the hanging drop, sitting drop and micro batch techniques. Urea was tested because it was present in the additive screen (with succinic acid pH 7.0 and 20% PEG 3350) and showed to decrease protein nucleation in the drops. Optimal conditions were found for the reducing agent TCEP and were later used to co-crystallize NapAB with other reducing agents: sodium dithionite and methyl viologen. DTT was no longer used for incubation due lack of suitable crystallization results.

For the soaking experiments, we used a harvesting buffer solution (HB) containing 25% PEG 3000, 0.1 ammonium citrate pH 5.5 and the ligands in a similar concentration as in the co-crystallization assays. The precipitant concentration was higher than in the crystallization assays in order to prevent the crystals to dissolve. The soaking experiments were made either by transferring single crystals to new drops containing the HB or by gently exchanging the mother-drop solution in which the crystals grew by the HB solution. The last method was performed by repeatedly adding between

**Table 2-1: Summary of ligands used in the co-crystallization assays: reducing agents, substrates, substrate- analogues and inhibitors.**
In parentheses the chemical formulas, underlined the acronyms and below the 2D structure of the compounds. Potassium cyanide, potassium thiocyanate, and sodium azide, perchlorate and carbonate where expected to act as NapAB inhibitors/substrate inhibitors.

| **Co-crystallization as additives or soakings** | | **Co-crystallization by incubation**<br>**(Reducing agents)** |
|---|---|---|
| Potassium/Sodium Nitrate (K/NaNO$_3$)<br>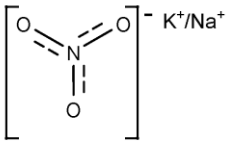 | Di-Potassium Carbonate (K$_2$CO$_3$)<br>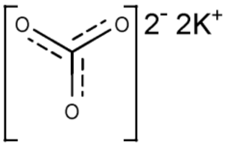 | TCEP - Tris(2-carboxyethyl)phosphine hydrochloride (C$_9$H$_{15}$O$_6$P)<br>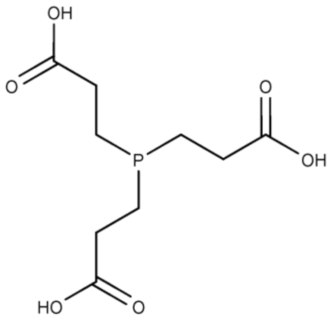 |
| Potassium Thiocyanate (KSCN)<br>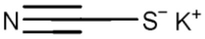 | Potassium Cyanide (KCN)<br>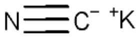 | |
| Urea (CH$_4$N$_2$O)<br>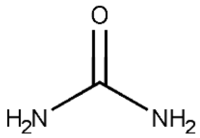 | Sodium Nitrite (NaNO$_2$)<br>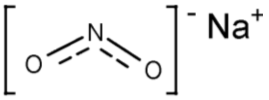 | Dit. – Sodium Dithionite (Na$_2$S$_2$O$_4$)<br>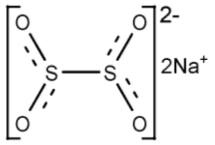 |
| Sodium Perchlorate (NaClO$_4$)<br>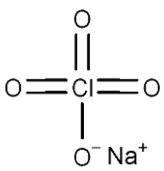 | Sodium Sulfite (Na$_2$SO$_3$)<br>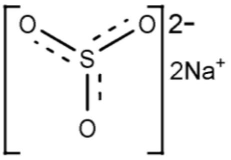 | DTT - Dithiothreitol (C$_4$H$_{10}$O$_2$S$_2$)<br>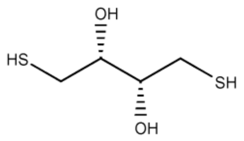 |
| Lithium Chloride (LiCl) | Sodium Azide (NaN$_3$) | MV - Methyl Viologen (C$_{12}$H$_{14}$Cl$_2$N$_2$) |

1 to 2 µL of the harvesting solution to the drop and then pipetting out the same volume from the drop no less than eight times. For soaking experiments longer than 10 minutes, a volume of 100 to 200µL from the same HB solution was added to the well and it was closed with the cover slip containing the crystals drop to prevent it from drying.

Crystallization trials were also performed inside an anaerobic chamber, in the absence of oxygen ($O_2$>70ppm). All the required material was deoxygenated with gaseous nitrogen for 15 minutes and introduced into the chamber after 3 vacuum cycles. After 30 minutes inside the chamber, the crystallization assays were started using the previously described procedure. Crystals grown in the anaerobic chamber were removed from the chamber and rapidly transferred to the harvesting solutions in an aerobic environment. The various compounds tested by co-crystallization and/or soaking are shown in **Table 2-1.**

Crystals were observed with a SteREO Discovery.V12 (Zeiss) microscope and those that seemed suitable for diffraction experiments (see below) were transferred to a cryo-protector solution containing 30% glycerol, 25% PEG 3000 and 0.1M ammonium citrate pH 5.5. We evaluated crystals morphology and size and chosen the ones with marked edges (over round-edged crystals) and crystals with suitable size for manipulation (> 0.1 mm) while avoiding multiple crystals. We were often able to choose crystals equal to or bigger than 0.1 mm in the smallest dimension. The crystals were rapidly incubated in the cryo-protecting solution and flash-frozen in liquid nitrogen in order to prevent ice crystals to form.

## 2.3 DATA COLLECTION, PROCESSING AND STRUCTURE DETERMINATION

The NapAB crystals were tested in-house using a Bruker D8 Venture dual source X-ray generator, a Photon 100 CMOS detector and an Oxford cryo-system. To achieve higher resolution data the crystals were also tested at several synchrotron facilities. Diffraction data were collected at the *European Synchrotron Radiation Facility* (ESRF – Grenoble, France) beamlines ID 29, 30B and at the *Diamond Light Source* (DLS – Harwell, United Kingdom) beamline I24.

For data reduction and indexing the programs iMOSFLM and XDS were used [39], [40]. For data scaling and merging the program AIMLESS from CCP4i2 suite was used [41], [42]. We evaluated the output observing the $CC_{1/2}$, I/σI and completeness values variations throughout resolution shells and determined for each dataset what resolution shells would be cut-off.

To solve the phase problem, molecular replacement was carried with PHASER [43] using a NapAB *Cn* model (PDB code: 3ML1) from which water molecules and other ligands were removed.

### 2.3.1 Model Building and Refinement

Refinement cycles were done with the REFMAC5 program [44]. For each data set, visual inspection and manual fitting were performed using the program COOT preceded by REFMAC5 cycles [44]. During refinement cycles, evaluation of the current model was assessed by observing the decrease and convergence of $R_{factor}$ and $R_{free}$, the number of outliers in the Ramachandran plots as well as visual inspections of the manually fitted atoms.

For adding water molecules into the refining models, the automatic water insertion command from COOT [45] was used followed by visual inspection of the electron density, temperature factor and distance to surrounding atoms.

For ligand insertion into the refining models, the ligand structure and restraints were obtained using the program COOT and the HIC-Up website. [45], [46].

## 2.4 THERMAL SHIFT ASSAYS (TSA)

We performed TSA using a real-time PCR system (StepOnePlus$^{TM}$- Applied Biosystems) and the Protein Thermal Shift Dye Kit$^{TM}$ [47]. Each reaction well (MicroAmp® Fast 96-well Reaction Plate 0.1 mL) contained: ligand solution varying in concentration, 1.7 mg/mL (15.8 µM) NapAB and of pre-diluted Dye solution as advised in the kit's protocol [47]. Temperature was initially stabilized to 25 °C for 2 minutes followed by a gradual increase to 99 °C for 50 minutes and another 2 minutes stabilization.

For each assay, the NapAB sample used was always fresh. Several ligands and reducing agents were tested and are summarized in **Table 2-2.** In the cases where NapAB was incubated with a reducing agent, its concentration was 10 % lower than in the non-incubation assays.

**Table 2-2: Summary of different conditions tested for NapAB *Cn* in TSA.** The first column indicates when NapAB was incubated for 20-30 minutes prior to the beginning of the assay. The second and third columns indicate what ligands and concentrations were tested. For the cases where no ligand was tested, the corresponding ligand volume (10µL) was buffer (Tris-HCl 300mM pH 7.6).

| Nap incubation | Ligand | Ligand concentration (mM) |
|---|---|---|
| - | $KNO_3$ | 2.5; 5; 10 |
| - | $NaNO_3$ | 2.5; 5; 10 |
| - | $KClO_4^-$ | 5; 10; 20 |
| - | TCEP | 2; 5; 10; 15; 35 |
| TCEP 14mM | $KNO_3$ | 5; 10; 20 |
| - | Dithionite | 5; 14; 20; 30; 40 |
| Dithionite 14mM | $KNO_3$ | 2.5; 5; 10 |
| Dithionite 20mM | $KNO_3$ | 2.5; 5; 10; 20 |
| Dithionite 30mM | - | - |
| Dithionite 30mM | $KNO_3$ | 2.5; 5; 10 |
| - | $NaNO_2$ | 2.5; 5; 10 |
| Dithionite 30mM | $NaNO_2$ | 2.5; 5; 10 |
| - | DTT | 5; 15; 20 |
| DTT | - | - |

## 2.5 ISOTHERMAL TITRATION CALORIMETRY (ITC)

Isothermal Titration Calorimetry was performed using a TA Instruments Nano ITC machine. Samples were placed in vacuum (25 °C) for 8 minutes before each assay to avoid any solid material in the samples. Reaction cell volume was 1 mL and stirring speed was 250 rpm.

We tested NapAB at 0.2 µM, 17.5 µM TCEP and titrated a 5 mM potassium nitrate solution. Six potassium nitrate injections of 15 µL were made into the reaction cell, varying the potassium nitrate concentration in the reaction cell between 74 µM and 412 µM.

## 2.6 MICROSCALE THERMOPHORESIS (MST)

We performed MST with a Monolith NT 1.115 (NanoTemper Technologies) and the Monolith NT™ Protein Labeling Kit RED - NHS was used to mark NapAB solvent accessible lysine residues. The buffer was exchanged to one provided by the kit (composition not known) in order to avoid the Tris buffer competition with the labeling reaction. The final concentration of the labelled NapAB sample was 4.4 µM. A series of preliminary tests were made to establish the optimal assay conditions. For an adequate signal, NapAB was diluted to 0.044 µM and 0,05 % Tween 20 (Polyoxyethylenesorbitan monolaurate) was added to the protein solution. Labelled NapAB samples were centrifuged at 9000 g for 10 minutes (4 °C) immediately before each assay and loaded into MST Premium Coated Capillaries (NanoTemper Technologies).

Binding affinity assays consisted of 16 different sodium and potassium nitrate concentrations. Two-fold serial dilutions produced the 16 different solutions for each assay and are presented in **Table 2-3.**

**Table 2-3 - MST Binding Affinity Assays.**
This table shows the ligand concentrations for capillaries 1, 2, 15 and 16 for each assay. Nitrate's counter ions potassium and sodium are varied for reasons explained in chapter 3.6.

| Capillary № | $NaNO_3$ (mM) | $KNO_3$ (mM) | $NaNO_3$ and $KNO_3$ (mM) | $NaNO_3$ (mM) | $NaNO_3$ (mM) |
|---|---|---|---|---|---|
| 1 | 300 | 500 | 1500 | 3000 | 4500 |
| 2 | 150 | 250 | 750 | 1500 | 2250 |
| 15 | 0.02 | 0.03 | 0.09 | 0.18 | 0.27 |
| 16 | 0.01 | 0.02 | 0.05 | 0.09 | 0.14 |

# 3 RESULTS AND DISCUSSION

## 3.1 PROTEIN PURIFICATION AND ACTIVITY ASSAYS

The NapAB protein was purified from an aliquot of previously isolated *Cupriavidus necator (Cn)* periplasm kept at -80 °C. Two chromatographic purification steps were performed using a cation exchange SP Sepharose column followed by a size exclusion Superdex 200 column (**Figure 3.1**).

Due to technical difficulties during the SP Sepharose HPLC, the corresponding chromatogram was saturated from the minute 54 onwards (data not shown). The collected fractions suspected to contain the NapAB elution were loaded on an SDS – PAGE gel for qualitative filtration. The fractions 39 – 53 contained the NapAB sample, and were pooled together and concentrated using a Macrosep (Pall corporation) of 30 kDa (**Figure 3.1.b**).

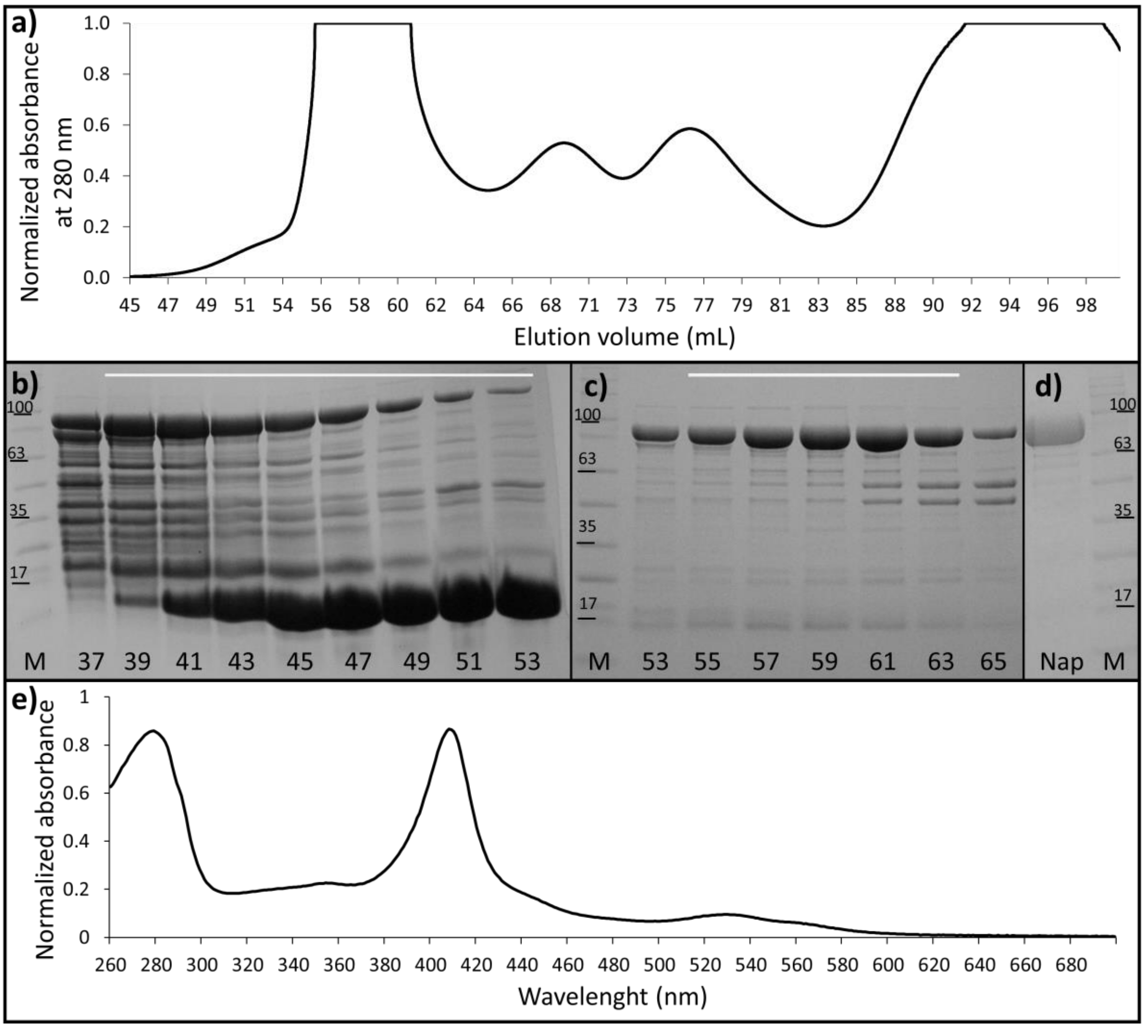

**Figure 3.1: Characterization of the NapAB purification.**
a) Chromatogram of the molecular exclusion Superdex 200 column (absorbance 280 nm). b-d) SDS-polyacrylamide gels of the purified NapAB. Results from the SP Sepharose (b) and from one of the three Superdex 200 chromatograms (c). The final NapAB sample (d) concentrated to 17 mg/mL. In all cases the NZY Color Protein Marker II was used and the 100, 63, 35 and 17 kDa marks are indicated. A white bar indicates pooled fractions for the main NapAB sample. e) Spectrum of native NapAB from 260-680 nm. The Soret band is visible at 409 nm.

Due to the large amount of NapAB obtained three separated runs (in similar conditions) were performed using the Superdex 200 column (**Figure 3.1.a)** in all cases followed by an SDS – PAGE for evaluation of the NapAB containing fractions. The resulting fractions 55-63 (**Figure 3.1.c**) were concentrated to a final concentration of 158 µM and the final buffer composition was 300 mM Tris-HCl pH 7.6. An SDS – PAGE of the final NapAB sample is shown in **Figure 3.1.d**. The NapAB concentration was calculated using the Soret band absorption at 409 nm (ε=212000 $M^{-1}$ $cm^{-1}$) in a spectrophotometer and in a plate reader. Aliquots of 250 µL, 100 µL and 50 µL were stored at -80 ºC for further usage.

To test for NapAB activity, a qualitative assay was performed using methyl viologen as the electron donor and sodium dithionite as reducing agent. The development of a very intense pink color after adding sulfanilamide and N-1-napthylethylenediamine dihydrochloride (NED) under acidic conditions confirmed the detection of the enzymatic reaction product nitrite in solution. This showed that the NapAB protein was fully active and able to be used in the further biochemical characterization assays.

The UV-Vis NapAB spectrum (**Figure 3.1.e**) contains the protein absorbance peak at 280 nm and the Soret band at 410 nm corresponding to the two heme groups, but lacks the iron-sulfur cluster characteristic absorbance between 350-500 nm due to the heme absorbance bands [16].

## 3.2 PROTEIN CRYSTALLIZATION

### 3.2.1 Screening and Optimization

#### *3.2.1.1 Bis-Tris and Succinic Acid*

We tested the previous successful *C. necator* NapAB crystallization conditions with PEG 3350 [16], [26] using 100 mM Bis-Tris pH 5.5 and 100 mM succinic acid pH 7.0, at 20 °C and NapAB at 158 µM. The PEG 3350 concentration was screened between 5 %, 10 % and 15 % (using Bis-Tris) and 10 %, 15 %, 20 % (using succinic acid). The condition with Bis-Tris did not result in any crystalline material while the succinic acid conditions contained needles, “urchins” and microcrystals when using 20% PEG. Following these results, we tested 100 mM succinic acid pH 7.0 with increased PEG 3350 concentration (25% and 30%) and lower NapAB concentration (80 µM.) In all cases drops were (1+1) and the reservoir contained 500 µL. When using 30 % PEG 3350 and NapAB at 158 µM the results showed protein amorphous precipitates while when using 25% PEG 3350 resulted in higher numbers of microcrystals (**Figure 3.2.a**). The NapAB dilution tests (80

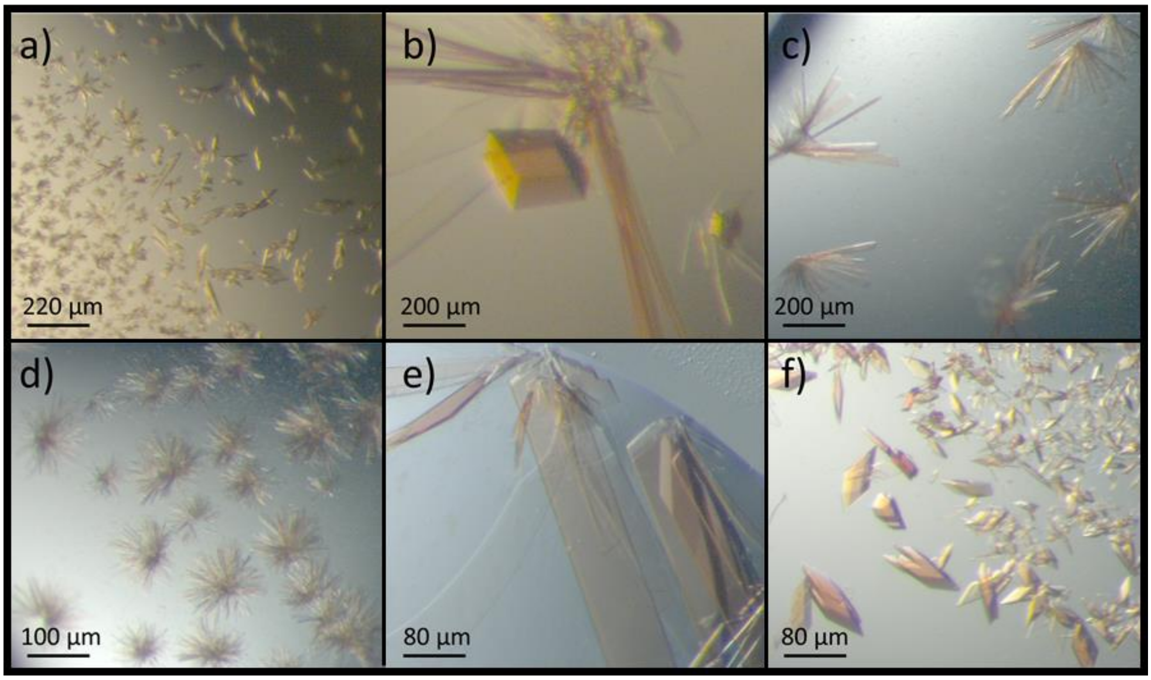

**Figure 3.2: Results from the crystallization screens.**
(a) Crystallographic results from the succinic acid condition (100 mM succinic acid pH 7.0, 25% PEG 3350; (b) from the additive screen, 12.5 mM urea as additive (100 mM succinic acid pH 7.0, 25% PEG 3350); (c-f) from the JCSG+ 200 mM Potassium formate, 20% PEG 3350 (d) 100 mM BICINE pH 9, 20% PEG 6000 (e) 200 mM Sodium thiocyanate, 20% PEG 3350 and (f) 100 mM Sodium citrate, 20% PEG 3000.

µM) showed a mixture of amorphous precipitates, needles and urchins for 25% PEG; needles and 2D crystals for 20 % PEG; and no precipitation for 15 % PEG.

We also tested the additive screen from Hampton research using 100 mM succinic acid pH 7.0, 20 % PEG 3350 and drops (1+0.25+0.75) corresponding to protein, additive and precipitant respectively. From this screen only 2 conditions resulted in significant crystalline material when using 0.1 M urea (**Figure 3.2.b**) and 0.1 M manganese chloride, to a final concentration of 12.5 mM in the drop. Urea seemed to act as a nucleation inhibitor, resulting in a well-defined crystal and a few needles originating from it. The manganese additive resulted in “urchins” with few crystals in the center.

### *3.2.1.2 The JCSG$^+$ screen*

In order to search for novel crystallization conditions, the JCSG$^+$ screen (96 conditions from Molecular Dimensions) was used manually and as a result a total of 28 different conditions provided promising results – including needles, “urchins” , 2D crystals and defective 3D crystals (**Figure 3.2.c-f**). The best results were from conditions containing 0.2 M ammonium citrate and 20% PEG 3350; and 0.1 M sodium citrate pH 5.5 with 20% PEG 3000 (**Figure 3.2.f**). Since so many conditions provided crystalline material (28 hits), the results were also interpreted from a statistical point of view from which the following was observed: 15 conditions (54%) contained 20% of PEG of any molecular weight; 14

conditions (50%) contained any concentration of PEG 3350; 10 conditions (36%) contained exactly 20% PEG 3350; 6 conditions (21%) contained citrate buffers.

These results led us to conclude that the major factors contributing to the high number of crystalline hits in the JCSG$^{+}$ screen was the presence of PEG 3000/3350 as the precipitating agent and its concentration ~ 20%. The number of hits containing citrate buffers were also considered significant. Therefore, we set on to test different PEG concentrations (15%, 20%, 25% and 30%), molecular weights (3000 and 3350) as well as citrate buffers (ammonium citrate and sodium citrate), in all cases using a pH of 5.5. The results corroborated that the most defining factor was the PEG concentration. Between PEG 3000 and 3350 no significant difference was observed and ammonium citrate produced slightly better results than sodium citrate. Using 30% and 25% PEG resulted in amorphous precipitate mixed with microcrystals; 20% PEG resulted in acceptable numbers of well-defined 3D crystals mixed with microcrystals; 15% PEG provided few or no crystalline material. We selected 100 mM ammonium citrate pH 5.5 and 20% PEG 3000 as the main crystallization condition in future experiments, using drops of (1+1), with 500 µL of the crystallization condition in the reservoir at 20 °C and initial NapAB concentration of 158 µM.

These results can be interpreted in a crystallization phase diagram, where PEG concentrations higher than 17.5% up to 25% gradually remain in the nucleation zone, stimulating the number of nucleus/crystals and lowering the average crystal size. Higher than 25% PEG concentrations reach the fast precipitation zone producing amorphous precipitates and lower PEG concentrations (<17.5%) gradually stay in the nucleation zone, producing a lower number of crystal nucleus, if any at all.

### 3.2.2 Co-crystallization with reducing agents

In an attempt to obtain the reduced form of Nap, the protein was incubated with reducing agents prior to crystallization. The first reducing agents to be tested were DTT and TCEP at 14 mM. The first preliminary results showed that no crystalline material was observed when using DTT. By contrary, when using TCEP an increase in nucleation resulting in higher amounts of smaller crystals was observed.

Various assays were made aiming to obtain crystals with DTT and optimize the crystals with TCEP. Potassium nitrate and urea were tested as additives for TCEP incubated NapAB co-crystallization assays. In contrast to urea, potassium nitrate seamed to improve the crystal size. Potassium nitrate was used because it was previously observed to significantly improve crystal size and decrease nucleation in other co-crystallization studies [15]. Urea was tested because it showed decreased nucleation when applied through the additive screen from Hampton Research as previously mentioned. However, this screen was only tested with the succinic acid crystallization condition and not with ammonium citrate.

Both vapor diffusion techniques (hanging and sitting drop) were tested in the search for the best crystallization condition, and we observed that using hanging drop provided more single crystals than sitting drop. Using a drop volume of (1.5+1.5) produced higher amount of suitable crystals than using (1+1) but was in average equal to (2+2). We chose (1.5+1.5) as the default drop volume to use for TCEP co-crystallizations since it produced similar results with expend of less amount of protein. We tested three different NapAB concentrations (126 µM, 111 µM and 79 µM – diluted from the initial 158 uM NapAB concentration) using 14 mM TCEP solutions or 300 mM Tris-HCl pH 7.6 as control. The results showed that a NapAB concentration of 126 µM was ideal for the TCEP co-crystallizations. By comparison with the controls we also noticed that NapAB concentration of 126 µM was best even for non-TCEP co-crystallization assays (we had previously tested NapAB concentrations of 158 µM and 80 µM). Crystallization at 4 ºC was also tested and

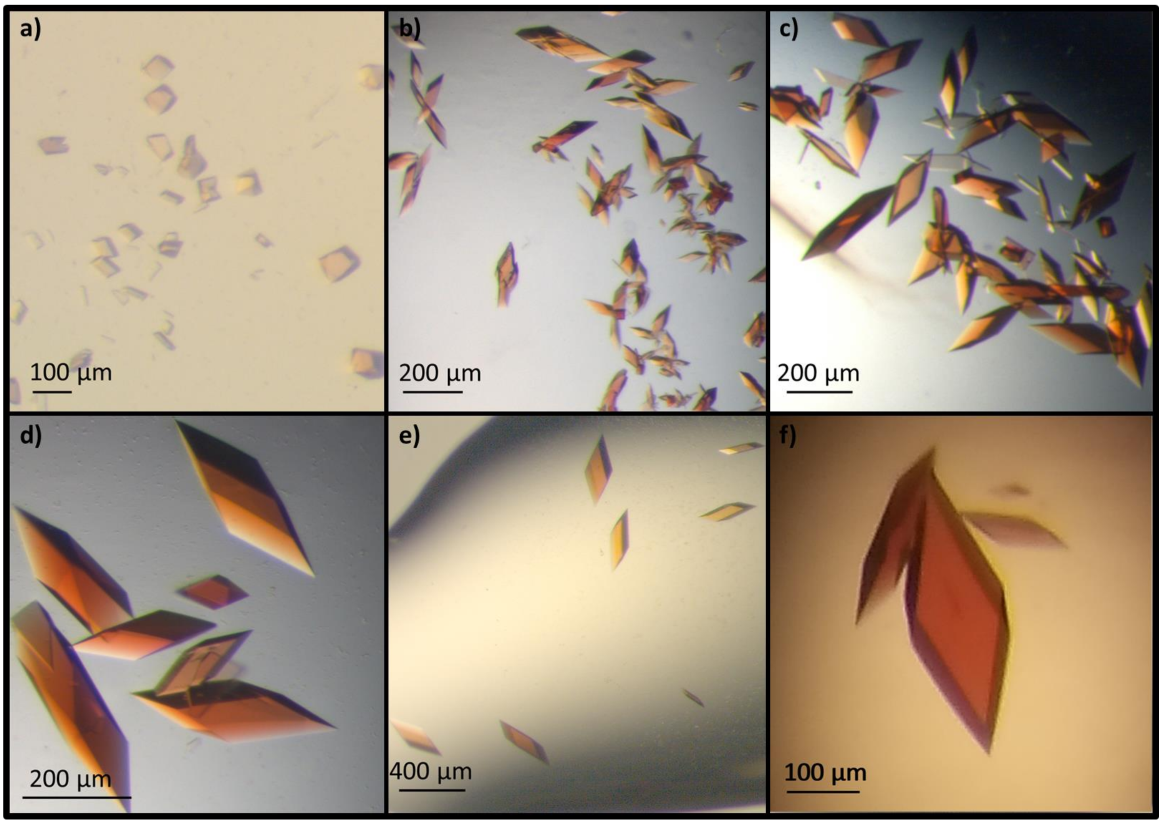

**Figure 3.3: Results from crystallization optimization and co-crystallization with DTT, TCEP and potassium nitrate.**
In all cases the buffer was 100 mM ammonium citrate pH 5.5. a) microbatch using mineral oil and 20% PEG 3000 and 158 µM Nap; b) 20% PEG 3000 and 158 µM Nap; c) 17.5% PEG 3000 and 158 µM Nap; d) 17.5% PEG 3000 and 126 µM Nap e) 17.5% PEG 3000 and 126 µM Nap co-crystallized with 100 mM potassium nitrate and 14 mM TCEP; f) 17.5% PEG 3000 and 126 µM Nap co-crystallized with 100 mM potassium nitrate in the anaerobic chamber.

resulted in a drastic increase of microcrystals for both native and TCEP co-crystallization assays.

The microbatch technique was also tested using mineral oil and (2+2) drop volume to try to maintain the reducing conditions when using TCEP and DTT. NapAB crystallization as well as co-crystallization assays with TCEP, DTT, potassium nitrate, TCEP with potassium nitrate and DTT with potassium nitrate were performed. Microbatch resulted in fewer and smaller crystals when comparing to hanging drop and was the only case were DTT co-crystallizations resulted in crystalline material, producing very small and round-edged crystals. (**Figure 3.3.a**).

We had previously tested PEG 3000 concentrations of 15%, 20%, 25% and 30% for native NapAB and opted to use 20% PEG as the default crystallization condition. Because TCEP induced nucleation, we retested the PEG concentrations this time for 15%, 17.5%, 20% and 22.5%. We noticed 17.5% PEG 3000 provided the best crystals for both TCEP incubated and native Nap, significantly increasing the crystal size.

By optimizing the co-crystallization of NapAB with TCEP, we fine-tuned the PEG concentration from 20% to 17.5% (**Figure 3.3.b-d**). The final optimized crystallization condition – 100 mM ammonium citrate pH 5.5, 17.5% PEG 3000 and 3 µL total volume drops – was used as the default until the end of this work. Co-crystallization of NapAB with TCEP slightly reduced the number of multiple crystals. Additionally, when potassium nitrate was used as additive in (1.5+0.5+1) drops, an increase in crystal size accompanied by a decrease of multiple crystals and numbers of crystals was observed (**Figure 3.3.e**). NapAB crystals grew to its maximum size in 7 days, with the first crystalline material appearing after the first 24 hours. The crystals grew to about 80% of their maximum size in 3 days and common crystal dimensions were 0.3 x 0.2 x 0.2 mm. This crystallization condition was also used for co-crystallization assays using sodium dithionite and methyl viologen and as a result both reducing agents showed a slight decrease in the number and size of crystals in the drop.

### 3.2.3 Other co-crystallization and soakings

A table with the effects that various ligands have on NapAB co-crystallizations assays is shown below (**Table 3-1**). Co-crystallizing with either sodium or potassium nitrate, in an attempt to obtain the crystals structure of the NapAB-substrate complex, significantly improved crystal size and decreased nucleation. This effect was observed even when using simultaneously the reducing agents TCEP, sodium dithionite and methyl viologen. We did not observe significant differences between sodium and potassium

**Table 3-1- Summary of the various NapAB ligands and effects in the co-crystallization experiments.**
In red are compounds that were used as reducing agents, in green the substrate and product of Nap and in blue other compounds like Nap inhibitors, substrate homologous or ligands from the additive screen used in this work. MV stands for methyl viologen and Dith for dithionite. (*) Crystals suitable for diffraction were only obtained when co-crystallizing with methyl viologen. (**) When using the microbatch technique, crystals were observed with a low degree of reproducibility.

| **Ligand** | **Verified effect in co-crystallizations** | **Structure obtained** | **Other comments** |
|---|---|---|---|
| $NaNO_3^-$ | Increase in crystal size; Nucleation inhibition | Yes | - |
| $KNO_3^-$ | | | |
| Dithionite | Induced Nucleation | Yes | - |
| $KNO_2^-$ | No significant effect observed | Yes | - |
| Methyl viologen | Induced Nucleation | Yes | Crystal breach openings during soakings |
| TCEP | Induced Nucleation; Crystal multiplicity reduction | Yes | - |
| Urea | Induced Nucleation | Yes | Nucleation inhibition verified only for the succinic acid crystallization condition |
| $MnCl_2$ | “Urchins” and crystals in the center | Yes | - |
| $K_2CO_3^{2-}$ | Needles / micro-crystals (*) | Yes | - |
| $KCN^-$ | No crystals | Only in soakings | - |
| $NaN_3^-$ | No crystals | Only in soakings | - |
| $NaSCN^-$ | Defective crystals | Only in soakings | - |
| $ClO_4^-$ | No crystals | No | - |
| DTT | No crystals (**) | No | - |
| $LiCl^-$ | Needles / micro-crystals | No | - |
| $Na_2SO_3^{2-}$ | Defective crystals | No | - |

nitrate, but noticed a slight increase in crystal size when comparing drops of (1.5+0.5+1) to (1+0.5+0.5).

Various NapAB inhibitors were used in co-crystallization and soaking assays with the objective of blocking or slowing catalysis, aiming to obtain the crystal structure of a NapAB reaction mechanism intermediary. We tested the NapAB inhibitor potassium cyanide [48] by co-crystallization and soaking. No crystals were obtained in the co-crystallization assays and NapAB crystals showed signs of degradation during the soaking experiments with potassium cyanide. We also tested sodium thiocyanate for the same purposes, although no crystals were obtained during co-crystallization assays, the soaking experiments did not result in the degradation signs that the cyanide soakings did.

We also attempted to co-crystalize NapAB with potassium carbonate, potassium perchlorate and potassium sulfite. Co-crystallization assays with potassium carbonate did not result in crystals suitable for diffraction but soaking NapAB crystals with potassium carbonate did not perturb the crystals. Also, crystals were obtained when co-crystallizing NapAB with methyl viologen and potassium carbonate. Co-crystallization assays with potassium perchlorate and potassium sulfite did not result in suitable crystals for diffraction.

Various crystallization assays were made in the anaerobic chamber. However, besides a lower degree of reproducibility, we did not observe any significantly difference when comparing crystallization assays in or out of the chamber (**Figure 3.3.f**).

## 3.3 DATA DIFFRACTION AND MODEL INTERPRETATION

We tested the NapAB crystals in-house using a Bruker D8 Venture dual source X-ray generator, a Photon 100 CMOS detector, and an Oxford cryo-system and the crystals diffracted to 3.3 Å maximum resolution. Because the objective of this work was to study the NapAB reaction intermediates, higher resolution structures were needed. To achieve higher resolutions, we sent the crystals to third generation X-Ray sources and diffraction data were collected at the European Synchrotron Radiation Facility (ESRF – Grenoble, France) beamlines ID 29, 30B, at the Diamond Light Source (DLS – Harwell, United Kingdom) beamline I24 and at the Deutsches Elektronen-Synchrotron (DESY – Hamburg, Germany) beamline P13 (PETRA III).

The majority of the crystals (summary in table 5 - 6) belong to space group *C*2 with unit cell parameters a = 135 Å, b = 71 Å, c = 114 Å and β = 110°. The only exception was a NapAB crystal consecutively soaked in several different solutions (first methyl viologen, followed by sodium dithionite, potassium nitrate and sodium azide) with the following unit

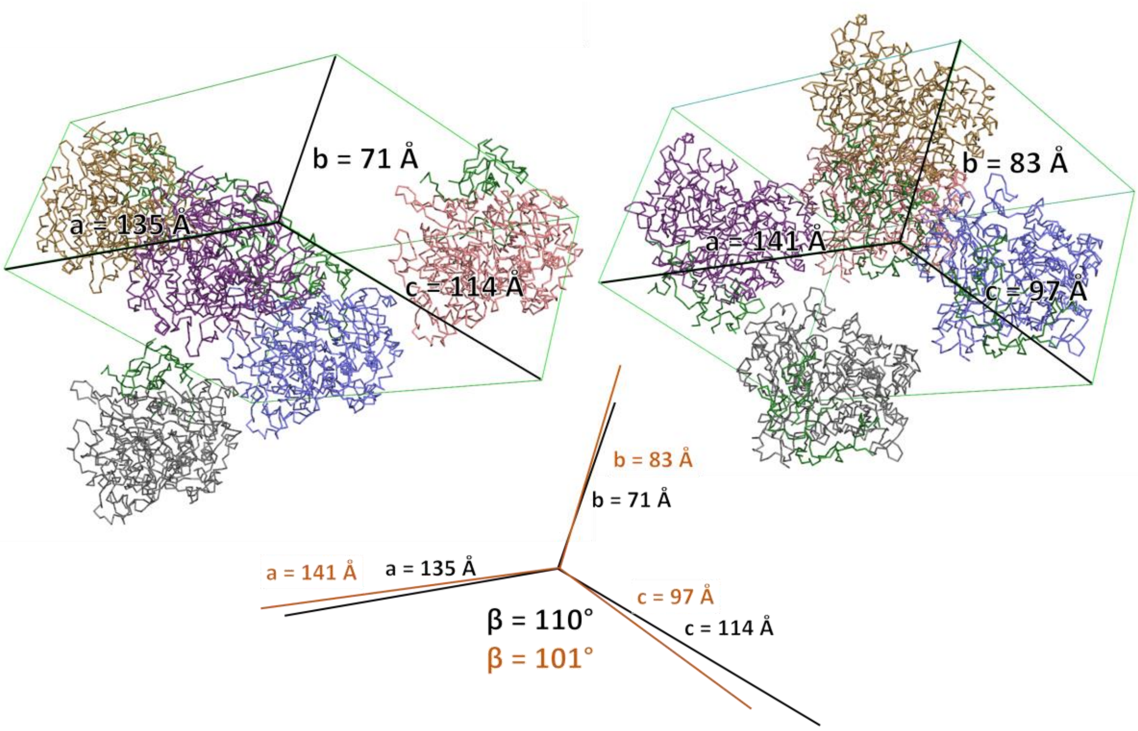

**Figure 3.4: Comparison of the different unit cells obtained.**
To the left a unit cell of a NapAB crystal obtained with 0.1 M ammonium citrate pH 5.5, 17.5% PEG 3000; the unit cell constants are also shown in black below. To the right, the unit cell of a NapAB crystal soaked in methyl viologen, followed by sodium dithionite, potassium nitrate and sodium azide; the unit cell constants are also shown in orange below. In the middle bellow is the comparison of the two unit cell constants.

cell parameters a = 141.6 Å, b = 83.2 Å, c = 97.3 Å and β = 101.3°. Interestingly, these unit cell parameters are similar to the parameters obtained by the previous NapAB studies (Coelho et al. 2007) using other crystallization conditions: a = 142.2 Å, b = 82.4 Å, c = 96.8 Å and β = 100.7°. Another NapAB study using ionic liquids resulted in different unit cell parameters from any structure obtained in this work, but also presented a space group C2 (a = 119.4 Å, b = 71.4 Å, c = 128.4 Å, b = 121.01°) [49]. All NapAB crystals sent to synchrotron beamlines are presented in tables **3.2** and **3.3**.

The NapAB crystals soaked first in methyl viologen followed by dithionite and potassium nitrate did not diffract whereas, similar crystals that received a final soaking in sodium azide did diffract up to 1.73 Å. These soakings had the intention of mimicking the activity assays were dithionite, methyl viologen and nitrate are used. It is possible that dithionite and methyl viologen pre-activate NapAB enabling catalysis to occur. When such crystals are soaked in the inhibitor sodium azide, the catalysis is prevented and the crystals may return to the original state and diffraction becomes possible again.

**Table 3-2 – Summary of the results from the Nap crystals obtained in aerobic conditions and tested in the various synchrotron beamlines.**

In red are compounds that were used as reducing agents, green the substrate and product of Nap and blue other compounds like Nap inhibitors or substrate analogs. MV stands for methyl viologen and Dith. for sodium dithionite. (*) Nap crystals whose diffraction data was collected without enough completeness to solve the structure. (**) Nap crystals that were sent to the synchrotron beamline but were not measured.

| Co-crystallization | | Soaking | Best res. (Å) | N° of tested crystals and soaking time | Beamlines |
|---|---|---|---|---|---|
| Incubation | Additive | | | | |
| - | - | - | 2.3 | 2 – HB 15min | ESRF ID29 |
| | | | | 2 – HB 9d | |
| | | | | 2 – HB 24d | |
| | | | | 1 | PETRA III P13 |
| | | $NaN_3^-$ | 2.1 | 2 – 5min | ESRF ID29 |
| | | | | 2 – 4d | |
| | | $KNO_3^-$ | 2.3 | 3 – 45min | ESRF ID30B |
| | | | | 4 – 20h | |
| | | MV | 2.2 | 2 | ESRF ID29 |
| | | MV → Dith.+ $KNO_3^-$ | No diffraction | 2 | |
| | | MV → Dith.+ $KNO_3^-$ → $NaN_3^-$ | 1.7 | 4 | |
| | | Dith. → Dith.+ $KNO_3^-$ | ** | 2 | |
| | | Dith. → Dith.+ $KNO_3^-$ → $KSCN^-$ | ** | 2 | |
| | $KNO_3^-$ | $KNO_3^-$ | * | 4 | ESRF ID30B |
| | | | * | 6 | |
| | Urea | $NaNO_3^-$ | * | 6 | |
| TCEP | - | $KCN^-$ | No diffraction | 1 | ESRF ID29 |
| | | TCEP | * | 4 – 5min | ESRF ID 30B |
| | | | No diffraction | 1 – 24h | ESRF ID29 |
| | | $NaN_3$ | No diffraction | 2 | |
| | | TCEP → $KNO_3^-$ | 2.0 | 3 – 24hTCEP 5min $KNO_3^-$ | |
| | $KNO_3^-$ | - | 1.8 | 5 | ESRF ID29/ DLS I24 |
| | | $KNO_3^-$ | 1.6 | 2 – 15min | ESRF ID29 |
| | | | | 2 – 1h | |
| | | | | 2 – 5h | |
| | | | | 2 – 2.5h | DLS I24 |
| | | $KCN^-$ | 1.9 | 2 – 5min | |
| | | TCEP | 2.1 | 4 – 5min | |
| | | | | 2 – 2h | |
| Dithionite | - | - | 1.7 | 2 | ESRF ID29 |
| | | $KNO_3^-$ | No diffraction | 2 | |
| | | MV | 2.1 | 3 – 24h | PETRA P13 |
| Methyl Viologen | - | MV | 1.8 | 2 – 5min | ESRF ID29 |
| | | | | 2 – 24h | PETRA P13 |
| | | Dith. | No diffraction | 2 | |
| | | Dith. → $KNO_3^-$ | 2.3 | 2 | |
| | $KNO_3^-$ | - | 1.6 | 3 | ESRF ID29 |
| | $K_2CO_3^{2-}$ | MV | 1.7 | 3 | |

**Table 3-3 – Summary of the results from the NapAB crystals obtained in anaerobic conditions.**

In red are compounds that were used as reducing agents, green the substrate and product of NapAB and blue other compounds like NapAB inhibitors or substrate homologous.

| Co-crystallization | | Soaking | Best res. (Å) | Nº of tested crystals and soaking time | Beamlines |
|---|---|---|---|---|---|
| Incubation | Additive | | | | |
| TCEP | $KNO_3^-$ | - | 1.9 | 2 | DLS I24 |
| | | $KNO_3^-$ | 2 | 2 | |
| | | TCEP | No diffraction | 2 | |
| | | TCEP → $KCN^-$ | 1.9 | 3 | |
| Dithionite | - | - | 2 | 5 | |
| | - | $KNO_3^-$ | 1.9 | 2 – 5min | |
| | | | | 2 – 15min | |
| | | | | 2 – 30min | |
| | $KNO_3^-$ | - | 2.0 | 2 | |
| | | $KNO_3^-$ | 2.0 | 2 | |
| | | $KNO_2^-$ | 2.2 | 2 | |

The NapAB crystals obtained from co-crystallization with methyl viologen often suffered damage during the soaking experiments. The crystals start to crack immediately after the soaking, but this could be regenerated after a few hours in the soaking conditions. Even crystals that were fast cooled with this type of damage, had recovered its initial appearance when observed again at the synchrotron beamlines. We also noticed significant differences between soaking the NapAB crystals with methyl viologen or co-crystallizing NapAB with methyl viologen. NapAB crystals soaked in methyl viologen and then soaked in sodium dithionite with nitrate did not diffract, whereas the NapAB co-crystallized with methyl viologen which were then soaked in sodium dithionite and nitrate did diffract up to 2.3 Å. If however no final nitrate soak was done, the same crystals did not diffract either. Additionally, dithionite co-crystallized NapAB crystals soaked in methyl viologen also diffracted up to 2.1 Å. Crystals that suffered damage during the soaking experiments with methyl viologen and recovered corroborate this hypothesis and suggest the structural change would be reversible. The fact that soaking or co-crystallizing NapAB with methyl viologen has different results also suggests that methyl viologen induces some kind of structural change in the crystal. However, we did not find significant structural changes when comparing the model with the one from the native crystal structure.

The previous *C. necator* NapAB studies showed a crystal structure where the Cys152, which coordinates the Mo atom, seems to adopt an alternate type of conformation corresponding to a partial reduced form of the enzyme [16]. This model corroborated the theoretical calculations made for elucidation of the reaction mechanism ([17], [18]). In our

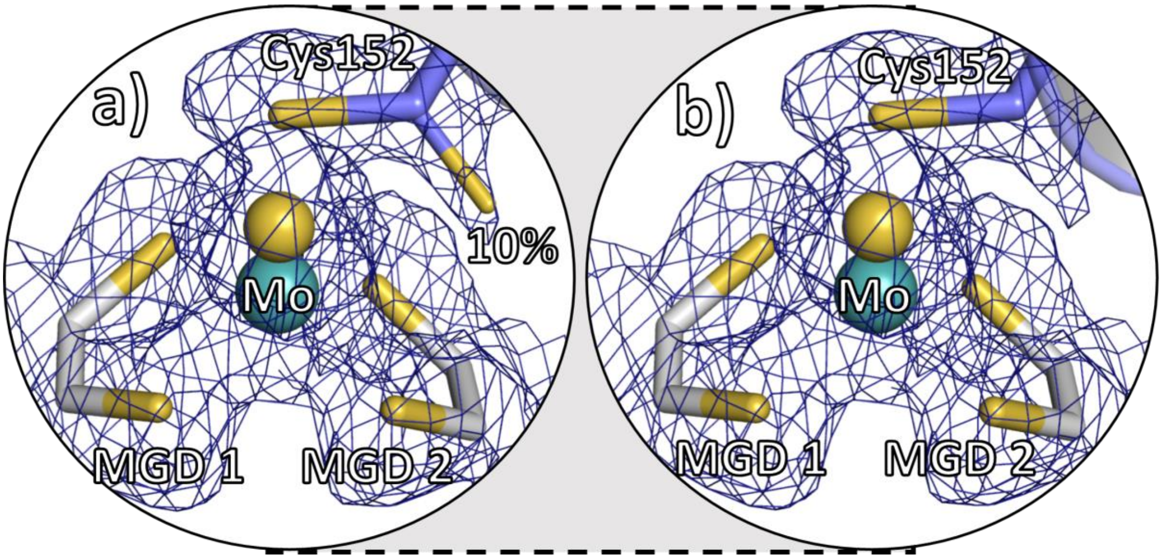

**Figure 3.5 - Crystal structure of partially reduced Nap and nitrite in nitrate co-crystallized Nap.**
This crystal structure was obtained by co-crystallizing Nap with TCEP and potassium nitrate in aerobic conditions. The statistics on data collection and refinement are presented in **Table 3-4**. Zoom in of cysteine 152 is shown. **a)** cysteine 152 and the occupancy of the alternate position. **b)** refinement of the same data as **a)** without the cysteine 152 alternate conformation. The electron density is contoured at 1$\sigma$.

studies, various co-crystallizations experiments using sodium dithionite and TCEP were made in order to obtain the reduced form of the enzyme. We found similar electron density in the Mo coordinating cysteine (**Figure 3.5**), suggesting an alternate conformation and further corroborating the previous studies.

Additionally, crystal structures in which nitrate was used in combination with one of the reducing agents (sodium dithionite or TCEP), a nitrite molecule was found in the cavity that leads to the active site of NapAB 12 Å from the Mo atom (**Figure 3.6**). This suggests that the crystallized NapAB is fully active, and that both sodium dithionite and TCEP are capable of pre-activating it. The NapAB spectrums with dithionite (**Figure 3.7**) corroborates this by showing a Soret band shift from 410 to 420 nm and the appearance of two bands at 550 nm and 522 nm that are characteristic of *c-type* heme reduction. However, the ITC results (explained below) seems to suggest that TCEP is not able to activate Nap. It is possible that both reducing agents can to some extent activate NapAB but at a drastically lower rate and/or efficiency, enough for the nitrite molecules to be detected in crystal structures (after several days since the crystals' growth until reaching synchrotron beamlines), but insufficient for the activity assays.

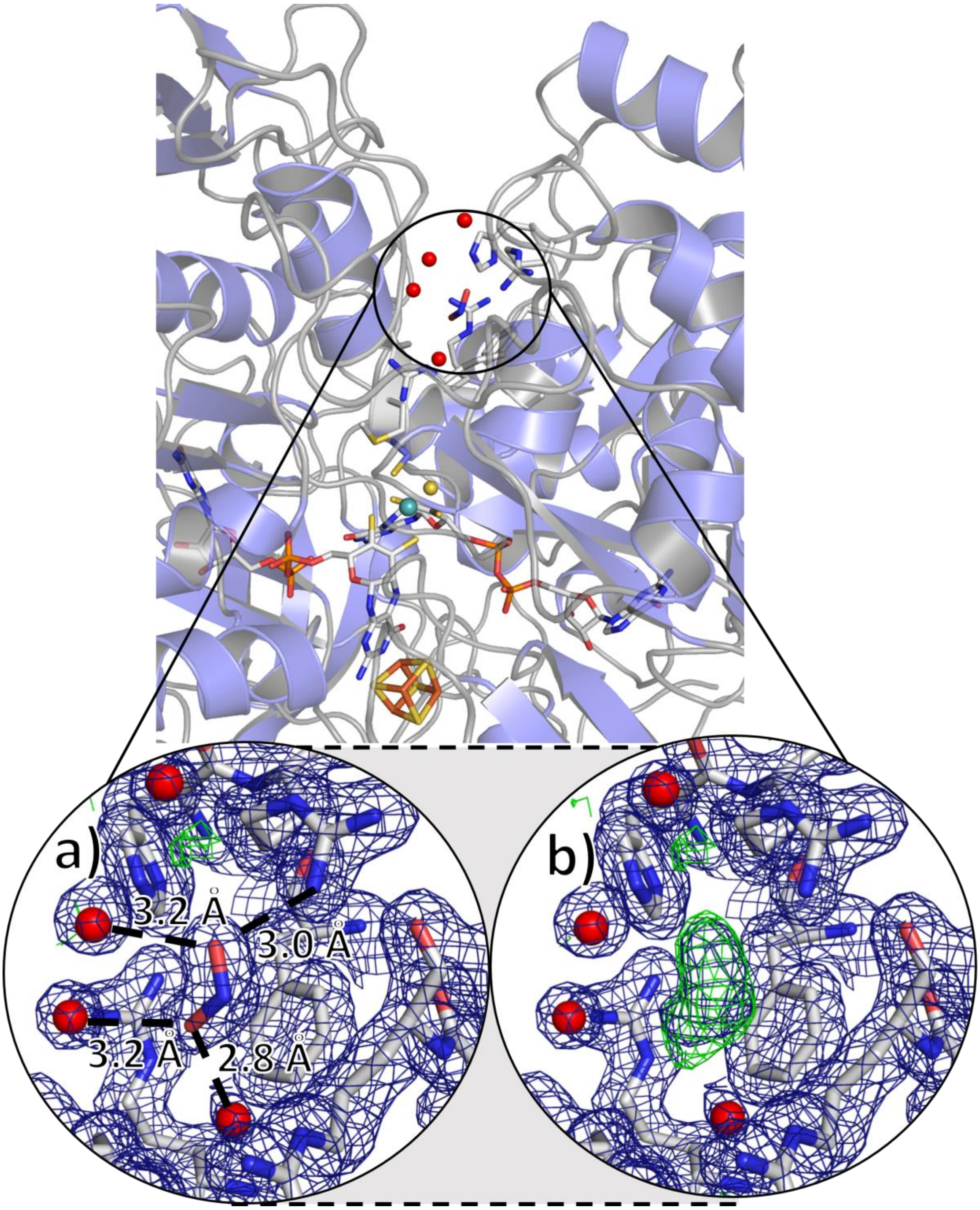

**Figure 3.6: Crystal structure of nitrite in nitrate co-crystallized Nap.**
This crystal structure was obtained by co-crystallizing Nap with TCEP and potassium nitrate in anaerobic conditions. The statistics on data collection and refinement are presented in **Table 3-4**. Zoom in of the nitrite molecule is shown. **a)** nitrite molecule and distances to the closer surrounding atoms. The average B factors of the nitrite molecule is 33, surrounding waters 26 and amino acids 21 **b)** refinement of the same data as a) without a nitrite molecule.

### 3.3.1 Oxidized cysteines

In the previous studies of NapAB from *C. necator* cysteine 784 was found to be oxidized to sulfonic acid [16]. Also, cysteine 388 showed extra positive electron density

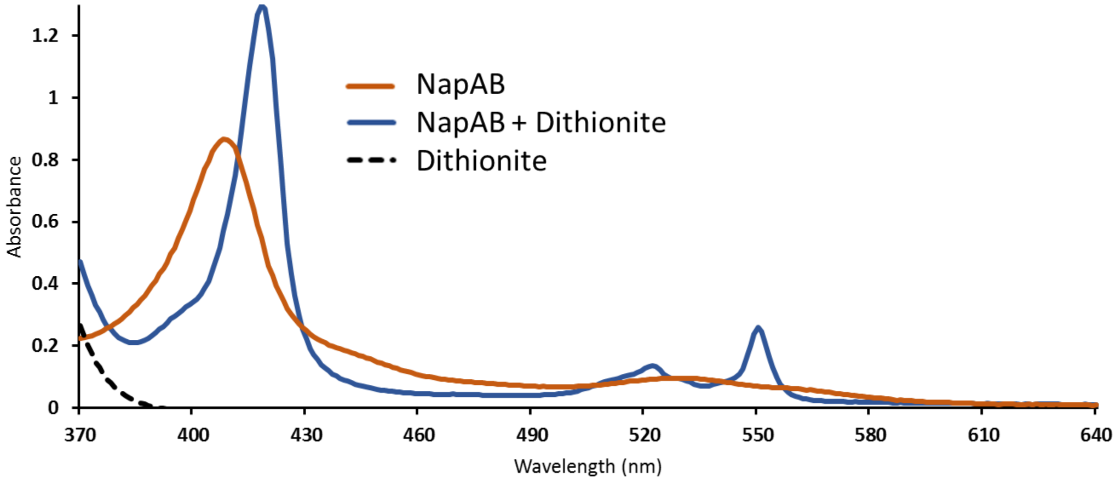

**Figure 3.7 : Spectrum of NapAB with sodium dithionite.**
The spectrum of NapAB is shown in orange, NapAB with 14 mM sodium dithionite in blue and 14 mM sodium dithionite in dashed black. A Soret band shift from 410 to 420 nm and the appearance of two bands at 550 nm and 522 nm are visible for the NapAB spectrum with sodium dithionite.

but to a lesser extent than cysteine 784 and was left unmodified. As indicated by Coelho et al. 2011, although cysteine 784 is not conserved, cysteine 388 is highly conserved among the periplasmic nitrate reductases. Both residues are solvent accessible, the cysteine 784 is located at the entrance to the channel that leads to the active site whereas cysteine 388 is located in the same channel, but closer to the active site – only 10 Å from the Mo atom (**Figure 3.8**). Because the oxidation of amino acids might have functional roles, namely as redox-sensitive regulatory switches [16], [50]–[52], we verified all the cysteine and methionine residues in the structures (the NapAB from *C. necator* has 14 Cys and 25 Met residues in total). No other Cys/Met residue showed this type of oxidation. This might also be related with the radiation damage from the X-rays, as ionizing radiation is known to lead to the oxidation of cysteines and methionines. It is known that the X-rays can lead to hydrogen peroxide formation, which reacts with cysteines resulting in sulfenic acid (CySOH). After the formation of sulfenic acid, further oxidation can occur to sulfinic acid (CySO2H) and then sulfonic acid (CySO3H) [53].

In our studies, we confirmed that NapAB co-crystallization with sodium dithionite resulted in the cysteine 784 being oxidized to sulfonic acid (**Figure 3.8**). We also observed the same effects in the TCEP co-crystallizations, however in the co-crystallizations using methyl viologen we found a more pronounced extra positive electron density for cysteine 388. We refined cysteine 784 as sulfonic acid and cysteine 388 as sulfinic acid (**Figure 3.8**). We also found that in structures obtained from crystals growth in the anaerobic chamber, both cysteine residues 784 and 388 lacked any extra positive electron density

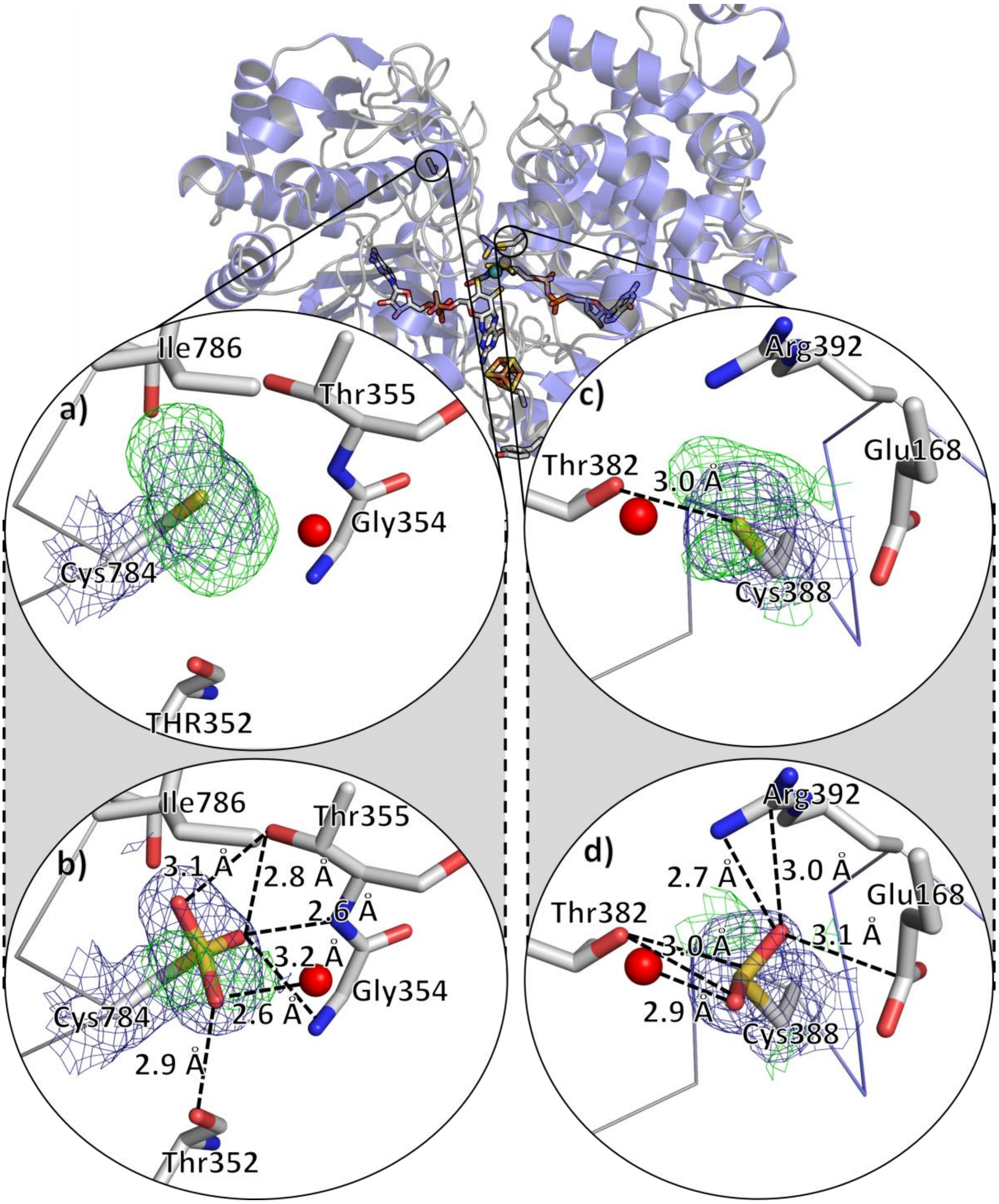
Ile786
Thr355
a)
Gly354
Cys784
THR352
Arg392
c)
Thr382
3.0 Å
Glu168
Cys388
Ile786
Thr355
b)
3.1 Å
2.8 Å
2.6 Å
3.2 Å
Gly354
Cys784
2.6 Å
2.9 Å
Thr352
Arg392
d)
2.7 Å
3.0 Å
Glu168
Thr382
3.0 Å
3.1 Å
2.9 Å
Cys388

**Figure 3.8 : Crystal structure of Nap zooming the oxidized cysteines 388 and 784 in the subunit NapA.**

This crystal structure was obtained by co-crystallizing Nap with methyl viologen and potassium nitrate. The statistics on data collection and refinement are presented in **Table 3-4.** Zoom in of cysteines 388 and 784 are shown and the temperature factors for each atom of the main chain, including alpha carbons. a) cysteine 784. b) cysteine 388. c) cysteine 784 refined as sulfonic acid. d) cysteine 388 refined as sulfinic acid.

that might suggest their oxidation. It is possible that in an anaerobic environment, the reaction that results in hydrogen peroxide formation ($Na_2S_2O_4 + O_2 + H_2O \rightarrow 2NaHSO_3 + H_2O_2$) is non-existent and therefore, oxidation of the cysteine 388 and 784 is not observed. The electron density of cysteine 152 in structures obtained from anaerobic growth crystals that were co-crystallized or soaked with TCEP or sodium dithionite was however still observed, corroborating an alternate conformation for TCEP or dithionite co-crystallizations. We also solved a few structures by cutting-off diffraction patterns collected

**Table 3-4: Statistics on data collection and structure refinement.**
Values in parenthesis correspond to the highest resolution shell. $R_{free}$ was calculated for 5% of the reflections randomly chosen for each data set. (*) MV (methyl viologen) was 14 mM, Dith. (sodium dithionite) was 14 mM, potassium nitrate was 100 mM and sodium azide was 100 mM. This structure was not fully refined.

| Parameters | TCEP AND $KNO_3$ (ANAEROBIC) | NATIVE CRYSTAL AND VARIOUS SOAKINGS (*) | MV AND $KNO_3$ |
|---|---|---|---|
| Synchrotron (beamline) | ESRF (ID-29) | DLS (I24) | RSRF (ID-29) |
| Wavelength (Å) | 0.99 | 0.99 | 0.99 |
| Space group | *C*2 | *C*2 | *C*2 |
| Unit cell parameters - a (Å); b (Å); c (Å); β (°) | 135; 71; 114; 110 | 142; 83; 97; 101 | 136; 72; 114; 110 |
| Number of molecules in the asymmetric unit | 1 | 1 | 1 |
| Matthews coefficient ($Å^3$ $Da^{-1}$) | 2.38 | 2.63 | 2.43 |
| Solvent content (%) | 48.3 | 53.2 | 49.5 |
| Resolution (Å) | 65.0 - 1.9 | 2.0 | 47.9 – 1.6 |
| Highest resolution shell (Å) | 9.8 – 1.9 | 10.1 – 2.0 | 8.76 – 1.6 |
| Number of observations | 253 193 (9 312) | 160 703 (10 554) | 690 137 (34 736) |
| Number of unique observations | 77 894 (4 144) | 71 556 (4 380) | 134 308 (6 664) |
| Multiplicity | 2.8 (2.2) | 2.6 (2.3) | 5.1 (5.2) |
| $R_{merge}$ (%) | 6.4 (28.0) | 7.0 (0.5) | 6.2 (74.0) |
| $R_{meas}$ (%) | 9.0 (39.1) | 10.0 (0.6) | 7.8 (93.0) |
| $R_{pim}$ (%) | 6.1 (27.0) | 7.4 (0.4) | 4.6 (41.1) |
| Completeness (%) | 99.7 (94.0) | 97.0 (95.4) | 99.8 (99.8) |
| I/Iσ | 17.7 (2.7) | 22.3 (2.0) | 12.2 (1.9) |
| Mosaicity | 0.35 | 0.80 | 0.18 |
| $CC_{1/2}$ | 0.86 (0.75) | 0.99 (0.60) | 0.99 (0.79) |
| Refinement | | | |
| Number of reflections | 77 892 | 71 546 | 134 308 |
| $R_{factor}$ | 0.16 | 0.22 | 0.16 |
| $R_{free}$ | 0.2 | 0.26 | 0.19 |
| r.m.s.d. from ideal geometry | - | - | - |
| Bond lengths (Å) | 0.019 | 0,0166 | 0.021 |
| Bond angles (°) | 2.13 | 1,781 | 2.28 |
| Average b factors for all amino acids ($Å^2$) | 25.0 | 26.7 | 24.5 |
| Ramachandran outliers (%) | 0.7 | 0.67 | 0.6 |
| Nº of waters | 459 | 144 | 480 |
| Other molecules | $KNO_2$; 2 x Glycerol | - | Glycerol; sulfinic acid; sulfonic acid |

at the end of the diffraction experiment. By avoiding this data, we lowered the contribution from possible radiation damage to the model, but observed the same electron density for cysteine 388 and 784 in these structures.

## 3.4 THERMAL SHIFT ASSAYS

To study ligands interaction with the NapAB protein we performed thermal shift assay experiments, using several substrates, inhibitors and reducing agents. We started by using the standard protocol available in the Laboratory (with a final protein concentration of 2 µM). However, the initial results showed that this concentration was too low to obtain a significant noise free signal and we decided to use 16 µM instead as the final concentration of NapAB. Because the fluorescence intensity is dependent on the amount of hydrophobic amino acid residues interacting with the dye, this might be a consequence of the protein having few hydrophobic residues as in the case of small globular proteins. However, this is not expected from NapAB from *C. necator* since it is a 110 kDa globular protein (NapA – 90 kDa and NapB – 17 kDa).

The TSA profile of NapAB is represented in **Figure 3.9.a-b** in the native state and in the presence of several ligands, such as TCEP, methyl viologen, sodium dithionite, potassium nitrate, sodium nitrite and potassium perchlorate (in all cases triplicates were made). The denaturation profile of the protein shows a multi-peak TSA profile starting from 45 ºC onwards and we considered 51 ºC as the NapAB melting temperature or $T_m$. In the presence of both nitrate ($KNO_3$, green) and nitrite ($NaNO_2$, blue) the results show an altered denaturation profile of NapAB (**Figure3.9 a**). When using 14 mM of sodium dithionite there are no significant changes in the denaturation profile NapAB (neither when using other concentrations – data not shown). The TSA shows that using a 15 mM of TCEP results in a significant denaturation of the protein, indicated by the high fluorescence intensity in the beginning of the assay (**Figure3.9 b**). When using a lower concentration of TCEP (5 mM) the profile changes are not significant different form the results obtained without TCEP.

These results from NapAB incubated with TCEP at 15 mM were unexpected. In the crystallographic assays when using 14 mM TCEP it was noticed that it decreased the number of multiple crystals. Even more, the best overall crystal condition was using TCEP incubations with nitrate. However, this is probably explained by the difference of the TCEP/NapAB ratio, whereas in the crystallization assays it is about 90, for the TSA it reaches 940.

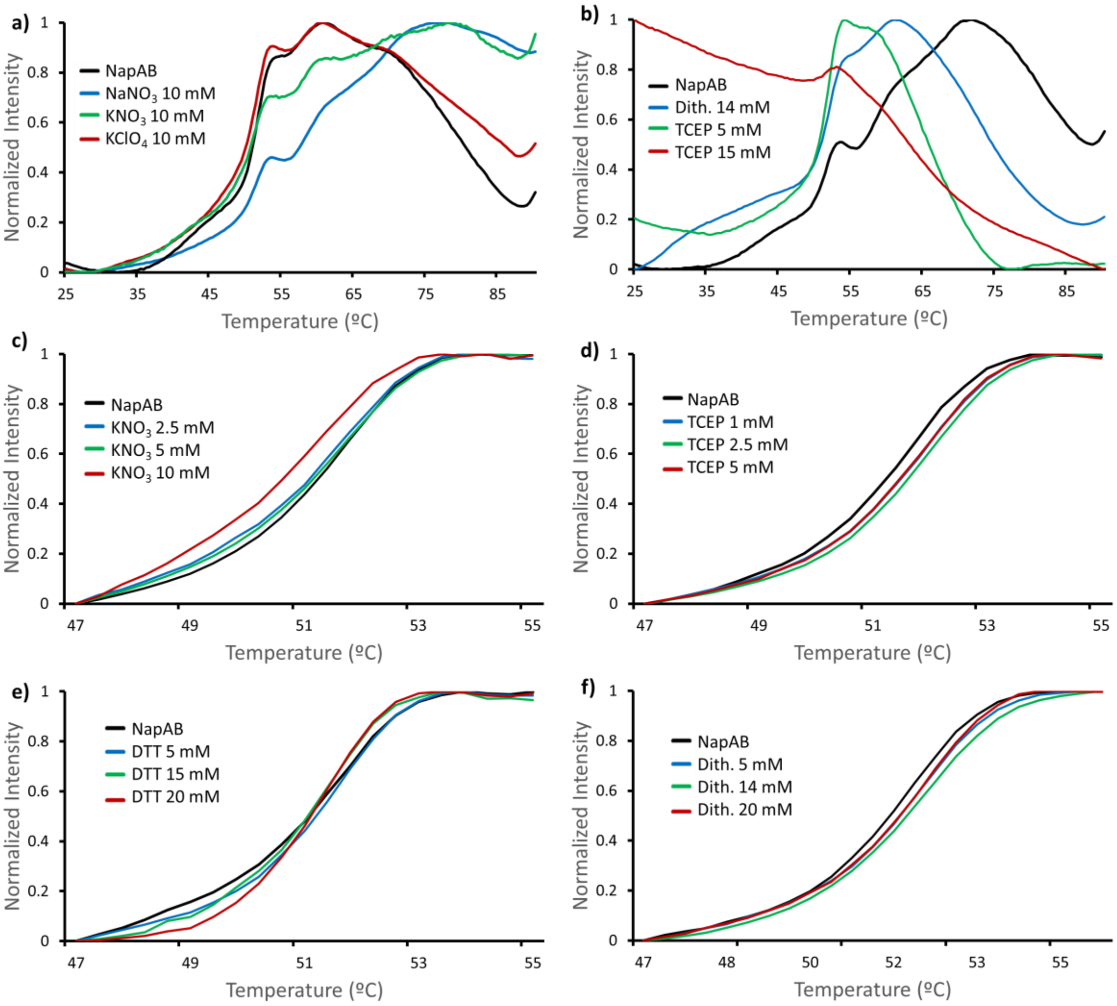

**Figure 3.9: Comparison of various TSA results.**

**a)** and **b)** show the native NapAB TSA profile and with potassium nitrite, potassium nitrate, potassium perchlorate, dithionite and TCEP; **c-f)** the NapAB melting curve using different potassium nitrate, TCEP, dithionite and DTT concentrations.

Most of the ligands tested resulted in minor alterations in the NapAB denaturating profile. This is visible when we compare the various melting curves (**Figure 3.9 c-f**) and observe no significant changes in the Tm for the various ligands tested. This shows that the protein is very stable in the purification buffer used (300 mM Tris-HCl pH 7.6) and that no significant structural changes are expected upon ligand binding in the crystal**)**. The presence of several different peaks in the NapAB profile might be due to different melting temperatures of the corresponding NapA and NapB subunits accompanied by different melting temperatures for specific NapAB domains. More studies are required to verify this hypothesis, including controls using an inactive form of the protein or the two subunits (NapA and NapB) isolated from each other.

## 3.5 ISOTHERMAL TITRATION CALORIMETRY

To try to obtain the thermodynamic parameters of the nitrate interaction with NapAB an ITC assay was carried out injecting TCEP and potassium nitrate into the reaction cell containing TCEP, potassium nitrate and Nap. In the control assay, NapAB was excluded from the reaction cell. We chose to test TCEP as the reducing agent because in the co-crystallizations structures obtained with TCEP a nitrite molecule was found near the active site channel, suggesting that TCEP might activate Nap. The fact that TCEP improved the crystallization of NapAB also contributed to this decision.

The ITC results (**Figure 3.10**) show that no nitrate-NapAB interaction or catalytic activity was detected. It might be that NapAB requires a suitable reducing agent not only for catalysis, but also for allowing nitrate-NapAB interactions. If TCEP is unable to pre-activate Nap, this would explain why neither catalysis nor nitrate-NapAB interaction was detected. To test this hypothesis, we performed a qualitative NapAB activity assay using TCEP instead of dithionite and methyl viologen. Interestingly we could not observe the development of a pink color corresponding to the presence of nitrite in solution, indicating that no nitrite was produced when using TCEP as the reductive agent and corroborating the ITC results that TCEP is not able to activate Nap. However, the crystal structures where nitrite was found were obtained using TCEP and nitrate co-crystallized, and this remains as a puzzling question.

More ITC experiments are required to better understand if ITC is a suitable technique to study NapAB reaction kinetics. So far there is no evidence in the literature that these assays have been performed on other bacterial nitrate reductases. The only study

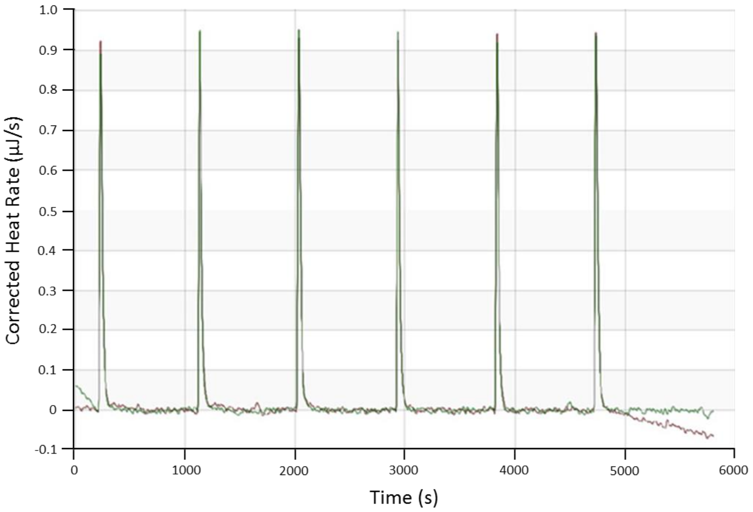

**Figure 3.10: Comparison of an ITC assay to the control.**
In the reaction cell was 0.2 µM NapAB and 17.5 µM TCEP (red line) and the control (green line) was absent of NapAB. Six potassium nitrate (5 mM) injections of 15 µL were made into the reaction cell, varying the potassium nitrate concentration in the reaction cell from 74 µM to 412 µM.

available refers to the eukaryotic NR where the authors study the Moco insertion into the apoenzyme [54]. Testing sodium dithionite or methyl viologen as reducing agents and electron donors, by mimicking the activity assays might be good starting choices for future assays.

## 3.6 MICROSCALE THERMOPHORESIS

In the MST assays, we initially tested two different labelled NapAB concentrations (4.4 µM and 44 µM) from which we could observe that the signal provided from the 44 µM sample was more adequate. Protein absorption to the capillary walls was observed when using the standard capillaries, but this problem was overcome when using the Premium Coated Capillaries as shown in **Figure 3.11.b** (NanoTemper Technologies).

We started by studying NapAB interactions with nitrate without the presence of any reducing agents. The first binding affinity test used potassium nitrate ranging in concentrations from 500 mM to 0.2 mM (**Figure 3.11.a**). This test seemed to detect nitrate interaction with Nap, suggesting that higher nitrate concentrations would be required for adequate $K_d$ calculation. We also tested potassium nitrite in similar concentrations but a loss in reproducibility was observed for all assays.

The first reproducibility problems concerned the lack of fluorescence homogeneity between capillaries, being proportionally higher with ligand concentrations. Within a couple assays, protein aggregation indicators became noticeable in the MST traces profiles. This is observable by the fluorescence regularity lack during the Infra-Red laser on stage (**Figure 3.11.d**).

Because the labelled NapAB sample showed aggregation, we centrifuged the sample prior to each assay at 9000 g for 10 minutes, and as a result the MST assays reveled a small degree of reproducibility, mainly in the MST traces. However, the capillary scans remained dubious. Because of this, we proceeded by testing if nitrate was non-specifically inducing fluorescence through the SDS denaturation test protocol provided by NanoTemper technologies.

We noticed that potassium salts are incompatible with the SDS test and so, we proceeded using sodium nitrate and later compared the results to verify that no significant differences were found between using potassium or sodium nitrate in the binding affinity tests. Ligand-dependent fluorescence changes can be originated from ligand-dependent protein absorption to labware (for example pipette tips), in which case detergent addition could help to solve the problem. After the SDS test confirming ligand-dependent fluorescence changes, we added Tween 20 detergent to the labelled NapAB sample to a final concentration of 0.05 %. By using this new approach (sample centrifugation and detergent usage) before the assays resulted in higher rates of reproducibility (**Figure 3.11.c**).

We tested different nitrate concentrations and observed that potassium and sodium nitrate provided similar results. However, in each assay the binding curve always suggested that higher ligand concentrations were required because too few dose response points were observable in the bound state. We experimented a few sodium nitrate concentrations and observed the same binding curve profile in every case, after which we stopped the MST experiments.

We concluded that the nitrate concentrations and calculable Kd ranges from those experiments were not biologically relevant. The Kd calculations were automatically estimated through the Monolith NT 1.115 software, which assumed one binding site for each ligand. In case this assumption is wrong for the NapAB study, this could explain the Kd ranges. However, the constant ligand-dependent fluorescence increase in the laser on stage, even at high nitrate concentrations contradicts this hypothesis. If the software would be responsible for the misleading Kd results, it would be expected that the ligand-dependent fluorescence increase would stop before reaching non-biologically relevant numbers.

Potassium and sodium nitrate behavior as salts, can explain the gradual increase in fluorescence. The MST signal change depends on three main factors: molecular size, charge and hydration shell. The titration of sodium and potassium nitrate, increasing the ionic strength in the capillaries might be responsible for the increase of fluorescence in the MST traces. To validate this hypothesis, a control test using different salts not expected to interact site-specifically with NapAB should be used in future assays.

During the experiments, we did not test NapAB with reducing agents. If NapAB is inactive without reducing agents, enzyme-substrate favorable interactions might be scarce when comparing to the active enzyme. Assays using combinations of dithionite and methyl viologen could be compared to the non-reduced NapAB results to verify such hypothesis. Experiments mimicking the activity assays in which Nap, nitrate and methyl viologen concentrations would be maintained, while titrating dithionite could provide valuable insight into the reaction mechanism. This method could avoid the concentration-dependent increase in fluorescence caused by nitrate, if it is a byproduct of the ionic strength escalation. The ionic strength in the capillaries should not significantly change during catalysis because, the substrate and product are both monovalent ions.

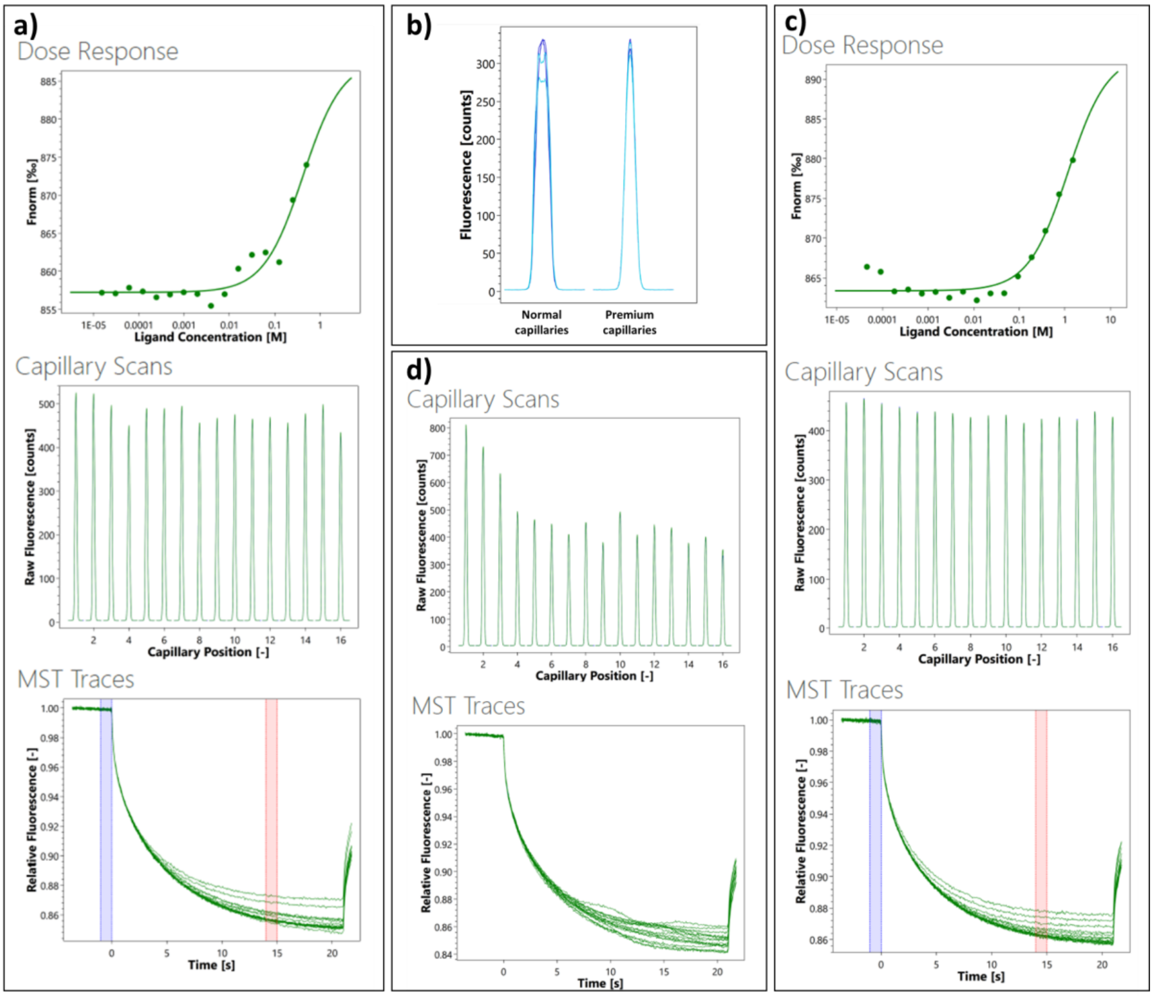

**Figure 3.11: Summary of the microscale thermophoresis assays.**
Dose response charts are calculated from the corresponding MST traces blue (laser off) and red (laser on) values. **a)** MST results for a potassium nitrate titration starting at 500 mM. The dose response chart shows the majority of data points in a unbound stage and few in the bound stage, suggesting at the time higher potassium nitrate concentrations should be used. In the capillary scans chart a 9% signal variation is shown. **b)** a capillary scan comparing Nap samples in normal or premium capillaries. In the first case capillary wall adhesion is observed. **c)** MST results for a sodium nitrate titration starting at 1500 mM, detergent was used to a final concentration of 0.05% and the samples were centrifuged prior to the assay. The dose response chart shows a similar result as in **a)**. In the capillary scans chart to 6% variation is shown. **d)** MST results for a sodium nitrate titration starting at 1500 mM, without using any detergent concentration or centrifuging prior to the assay. The capillary scans a signal variation of 67% is shown and in the MST traces signs of protein aggregation are observable in the laser-on region.

For future MST experiments, a strong control would be desirable. Proteins of similar sizes not related to nitrate, nitrite and the reducing agents dithionite or methyl viologen could be used. The ideal control would however be an inactivated NapAB protein.

# 4 CONCLUSIONS AND FUTURE PERSPECTIVES

During the course of this work, a total of 125 crystals were prepared and sent to various synchrotron beamlines, aiming to obtain a reaction mechanism intermediary structure of NapAB from *C. necator*. Complementing the X-Ray Crystallography study, we used three other techniques: TSA, ITC and MST. Although we did not obtain clear evidence for the reaction mechanism, we further advanced the case in study and paved the way for future experiments by optimizing the NapAB crystallization condition and the MST sample preparing.

During this work, we discovered and optimized a novel crystallization condition for NapAB from *C. necator*. The crystals grew with a high degree of reproducibility to approximate dimensions of 0.3 x 0.2 x 0.2 mm. The co-crystallization with potassium nitrate strongly improved the crystallization process, increasing the crystal size and inhibiting the nucleation event – which was commonly the bottleneck of the crystallization assays. Interestingly, although TCEP induced the nucleation event, when used in combination with potassium nitrate if further improved the crystals, significantly lowering the number of multiple crystals.

Coelho and co-workers obtained a partially reduced NapAB structure, where the coordinating Cys was found in two alternate conformations, one of which unbound from the Mo. This posed important implications on the discussion of the reaction mechanism for these enzymes. The structure was obtained using dithionite as the reducing agent and was the only such structure until now. In this work, we obtained similar electron density at the Mo coordinating cysteine for dithionite and TCEP co-crystallized NapAB. This corroborates the cysteine alternate conformation and therefore, the proposed mechanism suggests that TCEP is also suitable as a reducing agent to activate NapAB.

TCEP was used in the co-crystallization assays as well as in ITC and in TSA experiments. The TCEP and potassium nitrate co-crystallized NapAB structures show an alternate conformation of the Mo coordinating cysteine but also, a nitrite molecule at the substrate channel 12 Å away from the active site. This means that we have captured the structure of an intermediate state with the Cys partially displaced and the product nitrite on the substrate channel held by four H bonds. This further corroborates that TCEP is suitable to activate NapAB and provide the necessary reductive potential.

However, contrary to this evidence the ITC assays detect no catalysis or NapAB-nitrate interaction and the activity assays show no color development corresponding to the presence of nitrite in solution. This seems to suggest that TCEP is unable to activate NapAB when used as the single electron donor, making this a puzzling question. Possibly the reaction rate when using TCEP as the single electron donor is too low for detection by the activity assays. More ITC assays would help clearing this question. ITC assays testing sodium dithionite and methyl viologen as the electron donors should provide ITC signal correspondent to catalysis; otherwise, it becomes clear that ITC is not adequate for the study of NapAB.

Nitrite was also found in sodium dithionite and potassium nitrate co-crystallized NapAB. In the activity assays, the development of a pink color corresponding to the presence of nitrite is observable. The spectrum of NapAB with sodium dithionite show a Soret band shift from 410 to 420 nm and the appearance of two bands at 550 and 522 nm corresponding to of *c-type* heme reduction of NapAB. This strongly suggests that dithionite can activate NapAB when used as the single electron donor, even if at a slower rate that when used in combination with methyl viologen – the electron donor in the activity assay.

When methyl viologen co-crystallized NapAB crystals were introduced to soaking or cryoprotectant solutions, breaches were immediately formed. Often, the same crystals recovered from the breaches in a few hours, and even crystals fast-frozen (with the breaches) and sent to the synchrotron beamlines were there observed to lack any breach. The unit cell of one such crystal is different from all other unit cells obtained in this work, it has the cell constants of a = 141.6 Å, b = 83.2 Å, c = 97.3 Å and β = 101.3° in contrast to a = 135 Å, b = 71 Å, c = 114 Å and β = 110°. Moreover, NapAB crystals soaked in methyl viologen and then soaked in sodium dithionite with nitrate did not diffract, whereas the NapAB co-crystallized with methyl viologen which were then exposed to the same soakings did diffract up to 2.3 Å. The crystal cracking, the differences in unit cells and this difference in soaking results make it plausible that methyl viologen affects the crystal packing of NapAB. More co-crystallization assays using combinations of methyl viologen and sodium dithionite (mimicking the activity assays) might provide new insight on the reaction mechanism of NapAB.

Although MST did not provide any new insight, we did optimize the study of NapAB through MST. More MST and ITC assays may provide valuable information on this case study. Testing different combinations of sodium dithionite, sodium nitrate, methyl viologen and TCEP are interesting first choices for future experiments. Due to the NapAB crystal size using the novel crystallization condition (a 1,0 mm crystal was obtained), neutron diffraction might be a useful technique for the study of the reaction mechanism. Since proposed reaction mechanism involves the transfer of two protons (in two separated steps) to the active site that are released as water, information about them might become invaluable. Time-Resolved X-Ray Crystallography is also a technique with great potential for elucidating the reaction mechanism of NapAB. After optimization of adequate NapAB micro-crystals, various reaction mechanism intermediary structures along the catalysis are possible to obtain using this technique. If such structures are obtained, this technique may alone elucidate the reaction mechanism of NapAB.

From a personal perspective, this dissertation has completely fulfilled my expectations. It provided me extensive practical experience and a solid X-Ray Crystallography background, fulfilling its didactic role. Considering that X-Ray Crystallography is a technique of great potential and so vast, I am happy to consider myself a young novice crystallographer, with a satisfying understanding of the field and aiming to know more.

# 5 BIBLIOGRAPHY

[1] R. Hille, “Molybdenum and tungsten in biology,” vol. 27, no. 7, pp. 360–367, 2002.

[2] Y. Zhang and V. N. Gladyshev, “Molybdoproteomes and Evolution of Molybdenum Utilization,” pp. 881–899, 2008.

[3] R. R. Mendel, “Molybdenum Cofactor Biosynthesis and Molybdenum Enzymes,” 2006.

[4] C. Coelho and M. J. Romão, “Structural and mechanistic insights on nitrate reductases,” *Protein Sci.*, vol. 24, no. 12, pp. 1901–1911, 2015.

[5] M. J. Romão, “Molybdenum and tungsten enzymes: a crystallographic and mechanistic overview.,” *R. Soc. Chem.*, 2009.

[6] G. Schwarz, R. R. Mendel, and M. W. Ribbe, “Molybdenum cofactors , enzymes and pathways,” vol. 460, no. August, 2009.

[7] F. Bittner and R. R. Mendel, “Cell biology of molybdenum,” *Plant Cell Monogr.*, vol. 17, pp. 119–143, 2010.

[8] E. H. Perspectives, “Cycling out of Control,” *Environ. Health Perspect.*, vol. 112, no. 10, pp. 556–563, 2004.

[9] C. Sparacino-Watkins, J. F. Stolz, and P. Basu, “Nitrate and periplasmic nitrate reductases.,” *Chem. Soc. Rev.*, vol. 43, no. 2, pp. 676–706, 2014.

[10] J. F. Stolz and P. Basu, “Evolution of Nitrate Reductase : Molecular and Structural Variations on a Common Function,” vol. 15282, pp. 198–206, 2002.

[11] D. J. Richardson, B. C. Berks, D. A. Russell, S. Spiro, and C. J. Taylor, “Functional, biochemical and genetic diversity of prokaryotic nitrate reductases,” *Cell Mol Life Sci*, vol. 58, no. 2, pp. 165–178, 2001.

[12] J. M. Dias *et al.*, “Crystal structure of the first dissimilatory nitrate reductase at 1.9 Å solved by MAD methods,” *Structure*, vol. 7, no. 1, pp. 65–79, 1999.

[13] P. Arnoux *et al.*, “Structural and redox plasticity in the heterodimeric periplasmic nitrate reductase,” *Nat. Struct. Biol.*, vol. 10, no. 11, pp. 928–934, 2003.

[14] B. J. N. Jepson *et al.*, “Spectropotentiometric and structural analysis of the periplasmic nitrate reductase from Escherichia coli.,” *J. Biol. Chem.*, vol. 282, no. 9, pp. 6425–37, 2007.

[15] S. Najmudin *et al.*, “Periplasmic nitrate reductase revisited: A sulfur atom completes the sixth coordination of the catalytic molybdenum,” *J. Biol. Inorg. Chem.*, vol. 13, no. 5, pp. 737–753, 2008.

[16] C. Coelho, P. J. González, J. G. Moura, I. Moura, J. Trincão, and M. João Romão, “The crystal structure of cupriavidus necator nitrate reductase in oxidized and partially reduced states,” *J. Mol. Biol.*, vol. 408, no. 5, pp. 932–948, 2011.

[17] M. Hofmann, “Density functional theory study of model complexes for the revised nitrate reductase active site in Desulfovibrio desulfuricans NapA,” *J. Biol. Inorg. Chem.*, vol. 14, no. 7, pp. 1023–1035, 2009.

[18] N. M. F. S. A. Cerqueira *et al.*, “The effect of the sixth sulfur ligand in the catalytic mechanism of periplasmic nitrate reductase,” *J. Comput. Chem.*, vol. 30, no. 15,

pp. 2466–2484, 2009.

[19] H. Xie and Z. Cao, “Enzymatic reduction of nitrate to nitrite: Insight from density functional calculations,” *Organometallics*, vol. 29, no. 2, pp. 436–441, 2010.

[20] S. F. Sousa, N. M. F. S. A. Cerqueira, N. F. Brás, P. A. Fernandes, and M. J. Ramos, “Enzymatic ‘tricks’: Carboxylate shift and sulfur shift,” *Int. J. Quantum Chem.*, vol. 114, no. 19, pp. 1253–1256, 2014.

[21] N. M. F. S. A. Cerqueira, P. J. Gonzalez, P. A. Fernandes, J. J. G. Moura, and M. J. Ramos, “Periplasmic Nitrate Reductase and Formate Dehydrogenase: Similar Molecular Architectures with Very Different Enzymatic Activities,” *Acc. Chem. Res.*, vol. 48, no. 11, pp. 2875–2884, 2015.

[22] N. M. F. S. A. Cerqueira, P. A. Fernandes, P. J. Gonzalez, J. J. G. Moura, and M. J. Ramos, “The sulfur shift: An activation mechanism for periplasmic nitrate reductase and formate dehydrogenase,” *Inorg. Chem.*, vol. 52, no. 19, pp. 10766–10772, 2013.

[23] D. G. Rhodes, “Crystallography made crystal clear: A guide for users of macromolecular models (3rd Ed.),” *Biochem. Mol. Biol. Educ.*, vol. 35, no. 5, pp. 387–388, 2007.

[24] B. W. Matthews, “Solvent content of protein crystals,” *J. Mol. Biol.*, vol. 33, no. 2, pp. 491–497, 1968.

[25] A. Wlodawer, W. Minor, Z. Dauter, and M. Jaskolski, “Protein crystallography for aspiring crystallographers or how to avoid pitfalls and traps in macromolecular structure determination,” *FEBS J.*, vol. 280, no. 22, pp. 5705–5736, 2013.

[26] C. Coelho *et al.*, “Heterodimeric nitrate reductase (NapAB) from Cupriavidus necator H16: Purification, crystallization and preliminary X-ray analysis,” *Acta Crystallogr. Sect. F Struct. Biol. Cryst. Commun.*, vol. 63, no. 6, pp. 516–519, 2007.

[27] A. Wlodawer, W. Minor, Z. Dauter, and M. Jaskolski, “Protein crystallography for non-crystallographers, or how to get the best (but not more) from published macromolecular structures,” *FEBS J.*, vol. 275, no. 1, pp. 1–21, 2008.

[28] M. Levantino, B. A. Yorke, D. C. F. Monteiro, M. Cammarata, and A. R. Pearson, “Using synchrotrons and XFELs for time-resolved X-ray crystallography and solution scattering experiments on biomolecules,” *Curr. Opin. Struct. Biol.*, vol. 35, pp. 41–48, 2015.

[29] L. Mazzei, S. Ciurli, and B. Zambelli, *Isothermal Titration Calorimetry to Characterize Enzymatic Reactions*, 1st ed., vol. 567. Elsevier Inc., 2016.

[30] M. W. Freyer and E. A. Lewis, “Isothermal Titration Calorimetry: Experimental Design, Data Analysis, and Probing Macromolecule/Ligand Binding and Kinetic Interactions,” *Methods Cell Biol.*, vol. 84, no. 7, pp. 79–113, 2008.

[31] I. Faus *et al.*, “Isoprenoid Biosynthesis in Pathogenic Bacteria: Nuclear Resonance Vibrational Spectroscopy Provides Insight into the Unusual [4Fe-4S] Cluster of the E. coli LytB/IspH Protein,” *Angew. Chemie - Int. Ed.*, vol. 54, no. 43, pp. 12584–12587, 2015.

[32] M. Vivoli, H. R. Novak, J. A. Littlechild, and N. J. Harmer, “Determination of Protein-ligand Interactions Using Differential Scanning Fluorimetry,” *J. Vis. Exp.*, no. 91, pp. 1–13, 2014.

[33] L. Reinhard, H. Mayerhofer, A. Geerlof, J. Mueller-Dieckmann, and M. S. Weiss, “Optimization of protein buffer cocktails using Thermofluor,” *Acta Crystallogr. Sect. F Struct. Biol. Cryst. Commun.*, vol. 69, no. 2, pp. 209–214, 2013.

[34] M. K. Groftehauge, N. R. Hajizadeh, M. J. Swann, and E. Pohl, “Protein-ligand interactions investigated by thermal shift assays (TSA) and dual polarization interferometry (DPI),” *Acta Crystallogr. Sect. D Biol. Crystallogr.*, vol. 71, pp. 36–44, 2015.

[35] K. Huynh and C. L. Partch, “Analysis of Protein Stability and Ligand Interactions by Thermal Shift Assay,” no. February, pp. 1–14, 2015.

[36] M. Jerabek-Willemsen *et al.*, “MicroScale Thermophoresis: Interaction analysis and beyond,” *J. Mol. Struct.*, vol. 1077, pp. 101–113, 2014.

[37] P. Corporation, K. M. Miranda, M. G. Espey, and D. a Wink, “Griess Reagent System,” *Nitric Oxide*, vol. 5, no. 1, p. 7, 2009.

[38] H. Borcherding, S. Leikefeld, C. Frey, S. Diekmann, and P. Steinrücke, “Enzymatic microtiter plate-based nitrate detection in environmental and medical analysis.,” *Anal. Biochem.*, vol. 282, no. 1, pp. 1–9, 2000.

[39] T. G. G. Battye, O. Johnson, H. R. Powell, and A. G. W. Leslie, “iMOSFLM : a new graphical interface for diffraction- image processing with MOSFLM,” *Acta Crystallogr. Sect. D Biol. Crystallogr.*, pp. 271–281, 2011.

[40] W. Kabsch, “XDS,” *Acta Crystallogr. Sect. D Biol. Crystallogr.*, pp. 125–132, 2010.

[41] P. R. Evans and N. Garib, “How good are my data and what is the resolution ?,” *Acta Crystallogr. Sect. D Biol. Crystallogr.*, pp. 1204–1214, 2013.

[42] M. D. Winn *et al.*, “Overview of the CCP 4 suite and current developments,” *Acta Crystallogr. Sect. D Biol. Crystallogr.*, vol. 4449, pp. 235–242, 2011.

[43] A. J. Mccoy, R. W. Grosse-kunstleve, P. D. Adams, M. D. Winn, L. C. Storoni, and R. J. Read, “Phaser crystallographic software,” *Appl. Crystallogr.*, pp. 658–674, 2007.

[44] A. A. Vagin, A. Roberto, A. A. Lebedev, and S. Mcnicholas, “REFMAC 5 dictionary : organization of prior chemical knowledge and guidelines for its use,” *Acta Crystallogr. Sect. D Biol. Crystallogr.*, pp. 2184–2195, 2004.

[45] B. L. P. Emsley, W. G. S. And, and K. Cowtan, “Features and development of Coot research papers,” *Acta Crystallogr.*, pp. 486–501, 2010.

[46] G. Kleywegt, “HIC-Up,” 2017. [Online]. Available: http://xray.bmc.uu.se/hicup/. [Accessed: 01-Jan-2017].

[47] Life Technologies, “Protein Thermal Shift $^{TM}$ Studies,” *Protein Therm. Shift Stud.*, no. 4461808, pp. 7–34, 2011.

[48] S. a. Bursakov *et al.*, “Enzymatic Properties and Effect of Ionic Strength on Periplasmic Nitrate Reductase (NAP) fromDesulfovibrio desulfuricansATCC 27774,” *Biochem. Biophys. Res. Commun.*, vol. 239, no. 239, pp. 816–822, 1997.

[49] C. Coelho, J. Trincão, and M. Romão, “The use of ionic liquids as crystallization additives allowed to overcome nanodrop scaling up problems: A success case for producing diffraction-quality crystals of a nitrate reductase,” *J. Cryst. Growth*, vol. 312, no. 5, pp. 714–719, 2010.

[50] S. G. Rhee, K. Kim, and H. Z. Chae, “Irreversible Oxidation of the Active-site

Cysteine of Peroxiredoxin to Cysteine Sulfonic Acid for Enhanced Molecular Chaperone Activity *," vol. 283, no. 43, pp. 28873–28880, 2008.

[51] R. Radi, M. C. Kirk, S. Barnes, B. A. Freeman, and B. Alvarez, "Sulfenic Acid Formation in Human Serum Albumin by Hydrogen Peroxide and," pp. 9906–9914, 2003.

[52] N. Fujiwara *et al.*, "Oxidative Modification to Cysteine Sulfonic Acid of Cys 111 in," vol. 282, no. 49, pp. 35933–35944, 2007.

[53] J. A. Reisz, N. Bansal, J. Qian, W. Zhao, and C. M. Furdui, "Effects of Ionizing Radiation on Biological Molecules—Mechanisms of Damage and Emerging Methods of Detection," *Antioxid. Redox Signal.*, vol. 21, no. 2, pp. 260–292, 2014.

[54] P. Ringel *et al.*, "Biochemical characterization of molybdenum cofactor-free nitrate reductase from Neurospora crassa," *J. Biol. Chem.*, vol. 288, no. 20, pp. 14657–14671, 2013.